



Research Article

Process-driven microstructure design of 3D-Printed porous magnesium alloy scaffolds with tunable biodegradation kinetics

Weiyun Xu ^{a,b,1}, Hualuo Pang ^{a,1}, Haojing Xu ^a, Jing Liu ^{c,*}, Yufeng Zheng ^{d,**}, Peng Wen ^{a,***}^a State Key Laboratory of Clean and Efficient Turbomachinery Power Equipment, Department of Mechanical Engineering, Tsinghua University, Beijing, 100084, China^b Department of Civil and Environmental Engineering, University of Illinois Urbana-Champaign Urbana, IL, 61801, USA^c Applied Mechanics Laboratory, Department of Engineering Mechanics, School of Aerospace Engineering, Tsinghua University, Beijing, 100084, China^d School of Materials Science and Engineering, Peking University, Beijing, 100871, China

ARTICLE INFO

ABSTRACT

Keywords:
 3D printing
 Laser powder bed fusion
 High temperature oxidation
 Magnesium alloy
 Porous structure
 Biodegradation
 Microstructure design

3D-printed biodegradable magnesium (Mg) alloy scaffolds are emerging as promising candidates for customized bone implants, offering tailored structure, mechanical performance, and bioactive functions to address diverse bone defects. However, the premature loss of structural integrity remains a critical challenge for clinical applications due to the complex kinetics of biodegradation. This study posits that the tunability of degradation, inherently governed by microstructure, is rooted in the 3D printing and heat treatment processes, which have been underexplored and lack scientific understanding. Using a process-driven microstructural design approach, we investigated how manufacturing influence the corrosion behavior of porous Mg alloy scaffolds. By analyzing the combined effects of layer thickness on microstructural evolution in laser powder bed fusion and high-temperature oxidation heat treatment, it was revealed that the as-printed microstructural features, governed by the printing parameters, exert a critical influence on the biodegradable performance after heat treatment. Comprehensive evaluations of fusion quality, mechanical responses, electrochemical properties, and immersion degradation behavior further indicated that the multi-level heterogeneous microstructure, formed by local elemental migration, anisotropic grain growth, and the development of layered oxide films, was identified as the key factor in regulating degradation. Our findings highlight a synergistic manufacturing-dominant mechanism for tuning biodegradation kinetics through control of microstructure, resulting in porous Mg alloy scaffolds with significantly improved durability. These advancements not only provide a pathway for developing high-performance 3D-printed biodegradable bone implants but also establish a generalized framework for fabricating reactive materials with intricate geometries and tailored functionalities.

Nomenclature

(continued)

E_V (J/mm ³)	Volumetric energy input
E_L (J/cm)	Linear energy input
P_L (W)	Input laser power
S_V (mm/s)	Laser Scan speed
H_s (μ m)	Hatch space
LT (μ m)	Layer thickness
T_p (°C)	Preheat temperature
ρ_S (%)	Relative density of a solid

(continued on next column)

A_T (mm ²)	Total area of the measured region
A_D (mm ²)	Total area of defects
S_a (μ m)	Average height
S_q (μ m)	Root mean square height
S_z (μ m)	Maximum height
F (N)	Compression force
ΔL (mm)	Compression displacement
σ (MPa)	Engineering stress
ε (%)	Engineering strain

(continued on next page)

^{*} Corresponding author.^{**} Corresponding author.^{***} Corresponding author.E-mail addresses: thulijug@mail.tsinghua.edu.cn (J. Liu), yfzheng@pku.edu.cn (Y. Zheng), wepeng@tsinghua.edu.cn (P. Wen).¹ The authors contributed equally.

(continued)

A_0 (mm ²)	Initial cross-sectional area
L_0 (mm)	Initial height
E (GPa)	Young's modulus
σ_y (MPa)	Yield strength
I_{corr} ($\mu\text{A}/\text{cm}^2$)	Corrosion current density
E_{corr} (V)	Corrosion potential
R_p (k Ω)	Polarization resistant
H_P (μm)	Penetration depths of the melt pool
H_U (μm)	Uncovered deposition of the melt pool
H_P/LT (%)	Scale factor

1. Introduction

Magnesium (Mg) alloys have emerged as promising biodegradable materials for bone repair applications, offering unique advantages such as biocompatibility, osteoconductivity, and mechanical strength comparable to natural bone [1,2]. Recent advances in 3D printing technologies, particularly laser powder bed fusion (LPBF), have enabled the fabrication of intricate Mg alloy scaffolds to match patient-specific needs by tailoring geometries and the corresponding properties [3,4]. This capability positions Mg porous scaffolds as next-generation solutions for bone tissue engineering [5]. However, attributed to the larger specific surface area (i.e., the surface-to-volume ratio) and the more complicated microstructural characteristics, the degradation of 3D-printed porous Mg alloy scaffold is much faster than that of bulk structures by conventional manufacturing [6–8], which can cause early implant failures and has become the major challenge concerning real-world clinical applications. The biodegradation of Mg alloys, namely the corrosion in a body fluid environment, mainly occurs through electrolytic reactions with aqueous solution, resulting in the decline of mechanical integrity and the formation of loose Mg hydroxide and hydrogen gas bubbles [9]. Localized reactions can easily lead to an acceleration of overall degradation and structural collapse of Mg scaffolds [10]. In particular, LPBF is a layer-upon-layer fusion and deposition process, involving multiple possible formation defects and non-uniform microstructural evolution and having a tremendous impact on corrosion resistance [11]. Nevertheless, as chemically reactive alloys with significantly high vaporization tendency and diverse phase transformation processes, Mg alloys are substantially sensitive to processing parameters and conditions with respect to the formation quality during LPBF and resultant microstructure [12]. Therefore, studying the microstructural evolution driven by manufacturing processes and its impact on the degradation process holds significant scientific value for achieving stable service performance and realizing clinical applications of 3D-printed porous Mg alloy scaffolds.

The biodegradation kinetics of Mg alloys are intrinsically determined by two material aspects: the standard electrode potential (SEP) and the degradation products [13]. On one hand, the electrode potential of Mg is -2.37 V, which is lower than that of hydrogen and many other metallic elements, so that the Mg matrix reacts as the negative electrode in the electrolytic reaction, which generates degradation products composed of MgO, Mg(OH)₂, and hydrogen gas. On the other hand, MgO and Mg(OH)₂ are loose and lack a protective effect on the matrix; meanwhile, the hydrogen gas increases the local pH value, damages the integrity of the coating or passivation film, and further reduces the protective effect [14]. WE43 alloy, containing roughly 4 % Yttrium (Y) and 3 % Neodymium (Nd) + Gadolinium (Gd) in wt.%, exhibits high strength and corrosion resistance, and is one of the few Mg alloys that have achieved clinical applications, including bone screws [15] and vascular stents [16]. The inclusive rare earth (RE) elements in WE43 own atomic radii and electrode potentials similar to those of Mg, which can enhance thermodynamic stability and reduce the risk of electrochemical corrosion [17]. Moreover, these rare earth elements, particularly Y and Nd, react more preferentially than Mg and form dense rare earth oxides, thereby providing passivation protection for the Mg alloy matrix [18]. Besides the material composition, the macro-scale geometry also exerts

a fundamental influence on the degradation rate of Mg alloys. Featuring interconnected pores in the size of several hundred micrometres [19, 20], Mg alloy porous scaffolds can accelerate degradation by magnifying the exposure area between the immersion solution and the alloy [21]. Nevertheless, porous design can significantly affect the stress distribution inside the scaffold, while stress concentration can also accelerate the degradation by promoting pitting corrosion [22]. Among various scaffold designs, the fully-parameterized and 3D printing support-free triply periodic minimal surface (TPMS) structures are being favored in the bone regeneration field due to their smooth and negative curvature, balanced stress distribution, and geometry tunability [23,24]. Both microstructure and macro geometry of Mg scaffolds rely on a well-established 3D printing process along with its post-process [25]. However, it is still unclear how LPBF manufacturing and especially the following heat treatment processes affect the degradation of porous Mg alloy scaffolds.

The LPBF 3D printing process brings significant challenges to the precise control of Mg alloy degradation, with respect to formation quality and microstructural features that are both highly sensitive to process parameters such as layer thickness, laser power, scan speed and strategy, etc. [26]. Defects and deficiencies, such as cracks, porosity, and rough surface, can result in significant deterioration of degradation resistance [27]. Esmaily, M. et al. did a detailed analysis of 3D-printed WE43 showing that lack-of-fusion and keyhole porosity arising from insufficient or excessive energy input acted as preferential sites for localized corrosion, accelerating overall degradation in physiological media [28]. Quantitative map from energy density and scan strategy to build quality [29] also indicated that optimizing energy input reduces defects and corrosion current density, thereby enhancing corrosion resistance and mechanical retention. Furthermore, Mg alloys fabricated by LPBF generally exhibit heterogeneous grains and abundant precipitates, which promote the galvanic reaction and speed up the degradation [26,30]. Soderlind, J. et al. observed various columnar, dendritic, and banded microstructures of WE43 alloy by adjusting laser-scan parameters [31], which revealed the basic laser-magnesium interactions. Further study indicates that the corrosion rate of LPBF Mg alloy varies with the microstructural state, switching between fine equiaxed and coarse columnar/abnormally grown grains via Zr-induced columnar-to-equiaxed transition and Nd-mediated grain-boundary pinning [32]. Layer thickness, capturing the interplay between laser energy input and powder-particle dynamics, is reflected as a critical lever in LPBF to control the formation quality and microstructure evolution [33]. Yet, systematic investigations on its impact on porous Mg scaffolds are limited, and a clear process-microstructure-degradation linkage remains to be demonstrated.

Surface post-processes such as chemical conversion [34] and plasma electrolytic oxidation [35,36] are utilized to mitigate the degradation of Mg alloy by facilitating surface passivation. However, the intricate geometry of micro-pores within the porous scaffolds challenges the existing approaches to obtain uniform and reliable coating. To fully passivate via rare earth oxidation film, high-temperature oxidation (HTO) is developed, in which WE43 alloy is heated in an oxidizing atmosphere to enforce the outward diffusion of rare earth and form a dense and continuous protection layer of rare earth oxides *in situ* [37,38]. Compared with other surface coating methods, high-temperature oxidation is a stable, effective, and convenient treatment for complex porous structures; moreover, it does not introduce any other chemical components nor affect biocompatibility [39,40]. This heat treatment process enhances the performance of 3D-printed WE43 alloy via surface passivation and further gradient microstructural modification [41]. Our previous experiments found that the high-temperature oxidized LPBF Mg bulk samples, which were heated at 525 °C for 8 h, kept their structural integrity after 28-day static immersion [39]. In-vitro tests further confirmed the oxidation effect on biodegradation, with non-uniform rare-earth migration and recrystallization-induced coarsening leading to moderate grain growth [18]. However, rather than just

revealing the impact of HTO-induced microstructure on the degradation of Mg alloy, a systematic elucidation of how prior LPBF parameters govern the post-heat-treatment degradation properties has not been reported.

Overall, the degradation regulation of 3D-printed porous Mg alloys is governed by process sensitivity, coupled process-material-structure interactions, and multiple factors introduced by LPBF and subsequent high-temperature oxidation [42]. However, how the LPBF process parameters – particularly layer thickness – jointly with high-temperature oxidation determine the multi-level microstructure and, in turn, the degradation and mechanical properties of thin-walled porous Mg scaffolds remains insufficiently understood. In particular, the synergistic effect of LPBF and high-temperature oxidation and the role of the resulting multi-level microstructural distribution in controlling biodegradation have not yet been systematically elucidated. This knowledge gap limits our ability to deliberately tune the degradation kinetics of 3D-printed porous Mg alloy scaffolds.

To address this gap, the present work systematically investigates the mechanism underlying the synergistic “LPBF + HTO” process and conducts a process-parameter driven study centered on layer thickness, closely aligned with the unique characteristics of 3D-printed porous WE43 Mg scaffolds. Fig. 1a schematically illustrates our central hypothesis: although a subsequent high-temperature oxidation treatment is required, the as-printed state, directly controlled by LPBF parameters, pre-programs the final gradients in grain size/orientation and phase distribution within the scaffold, thereby enabling tunable degradation behavior. This concept, later validated in our study, presents a new trade-off mechanism between 3D printing and heat treatment in terms of microstructural evolution and distribution – while LPBF introduces a highly anisotropic grain structure, HTO mitigates this effect through recrystallization but simultaneously induces a stratified element distribution. This explicit process-microstructure-performance linkage, with layer thickness as the primary lever, has not been established in previous studies that treated LPBF optimization and post-treatments largely in isolation. As illustrated in Fig. 1b–g, we selected Gyroid TPMS structures as representative complex porous scaffolds and, by varying the printing layer thickness and oxidation conditions, deliberately produced distinct grain configurations and phase stratifications. Comprehensive material characterizations then revealed how these process-induced microstructural states govern mechanical properties, electrochemical responses, and static corrosion behavior. In particular, we demonstrate that an intermediate layer thickness yields an as-printed microstructure that, after HTO, forms a dense, uniform rare-earth-rich oxide layer and delivers significantly enhanced corrosion resistance. By uncovering this synergistic LPBF + HTO mechanism and showing that degradation kinetics can be tuned at the manufacturing stage via microstructural design, our findings advance microstructural engineering strategies for additively manufactured biodegradable metals and provide a practical pathway to fabricate porous Mg scaffolds with predefined, region-specific degradation timelines and mechanical responses for demanding medical applications.

2. Experimental section

2.1. LPBF-HTO process

WE43 Alloy Powder: For the 3D printing of porous structures, WE43 alloy powder was formed by plasma rotating electrode process (PREP). The powder is of 250 mesh size, with a distribution of 21.8 μm (D10), 40.3 μm (D50), and 64.5 μm (D90). The chemical composition of the powder, along with the LPBF-fabricated and subsequently high-temperature oxidized samples, was obtained via inductively coupled plasma optical emission spectroscopy (ICP-OES).

LPBF Fabrication: The porous TPMS Gyroid structures were additive-manufactured by a commercial LPBF system (BLT S210, China). The system is equipped with a laser source of 500 W power and 70 μm focus

spot diameter (IPG YLR-500, Germany), and a maximum 105 mm × 105 mm × 215 mm building space. The key indicators, volumetric energy input E_V and linear energy input E_L , are defined as

$$E_V = P_L / (S_V \times H_S \times LT) \quad (1)$$

$$E_L = P_L / S_V \quad (2)$$

where P_L is the input laser power, S_V is the scan speed of the laser, H_S is the hatch space, and LT is the layer thickness. During fabrication, the process chamber must be filled with pure argon shielding gas and maintain the oxygen content no higher than 120 ppm. A 35 mm thick rolled plate of WE43 alloy was used as the substrate (Movie S1). The substrate can be preheated to 200 °C selectively, which was set as a process parameter for investigation in this work. A zigzag laser scanning route with a 67° rotational offset angle between adjacent building layers was selected. After getting removed from the substrate, the as-built WE43 samples were chemically polished by a mixed acid solution (5 % HCl, 5 % HNO₃, and balanced C₂H₅OH, in volume) for 60–120 s to remove the sticky powder and achieve the target porosity [4, 40]. For clarity, the polished samples are referred to as LPBF samples in this paper.

High Temperature Oxidation: A digitally controlled box furnace (KSL-1200X, China) with circulating air was utilized to realize the high temperature oxidation (HTO) of WE43 alloy. With a heating rate of 8.33 °C/min, the LPBF samples were heated from room temperature to 525 °C, maintained for 8 h, and water quenched to room temperature [39]. For clarity, the oxidized samples are referred to as HTO samples in this paper.

2.2. Formation evaluation

Fusion Quality: The fusion quality of the fabricated TPMS structures was mainly characterized by the relative density ρ_S of the solid. Utilizing an optical microscope (Olympus DP-72, Japan), both the cross-sections perpendicular and parallel to the building direction of the as-built samples were observed. Thereby, ρ_S can be determined by

$$\rho_S = \frac{(A_T - A_D)}{A_T} \times 100 \% \quad (3)$$

where A_T is the total area of the measured region, and A_D is the area of defects (voids, inclusions, and unmelted region). In this study, an image processing algorithm was employed to pixelate optical microscopy images [29]. The number of pixels corresponding to the cross-section and defects was quantified separately using a Python script (see the Mendeleev Data repository), and the relative density was calculated accordingly. Meanwhile, the roughness and fluctuations of the cross-section boundaries were derived.

Surface Roughness: The surface roughness of LPBF and HTO porous structures was measured via a white light interferometer (Zygo Nextview™ NX2, US). According to ISO 21920-2:2021, three locations of curved surface for each sample were characterized to derive the corresponding average height S_a , root mean square height S_q , and maximum height S_z . The data were extracted using Zygo Mx™ software (version 9.2.0.1852) with default filter settings.

2.3. Microstructure characterization

Microscopic Morphology and Phase Composition: The microstructure of LPBF and HTO samples was characterized mainly by a scanning electron microscope (SEM, Zeiss Gemini-300, Germany), with the extra high tension (EHT, 15 kV) accelerating voltage setting. The microscopic morphology of both surface and cross-section was observed using a back-scattered electron (BSE) detector and a high-angle annular dark field (HAADF). At the same time, the atomic fractions of elements at regions of interest were measured via energy-dispersive spectroscopy

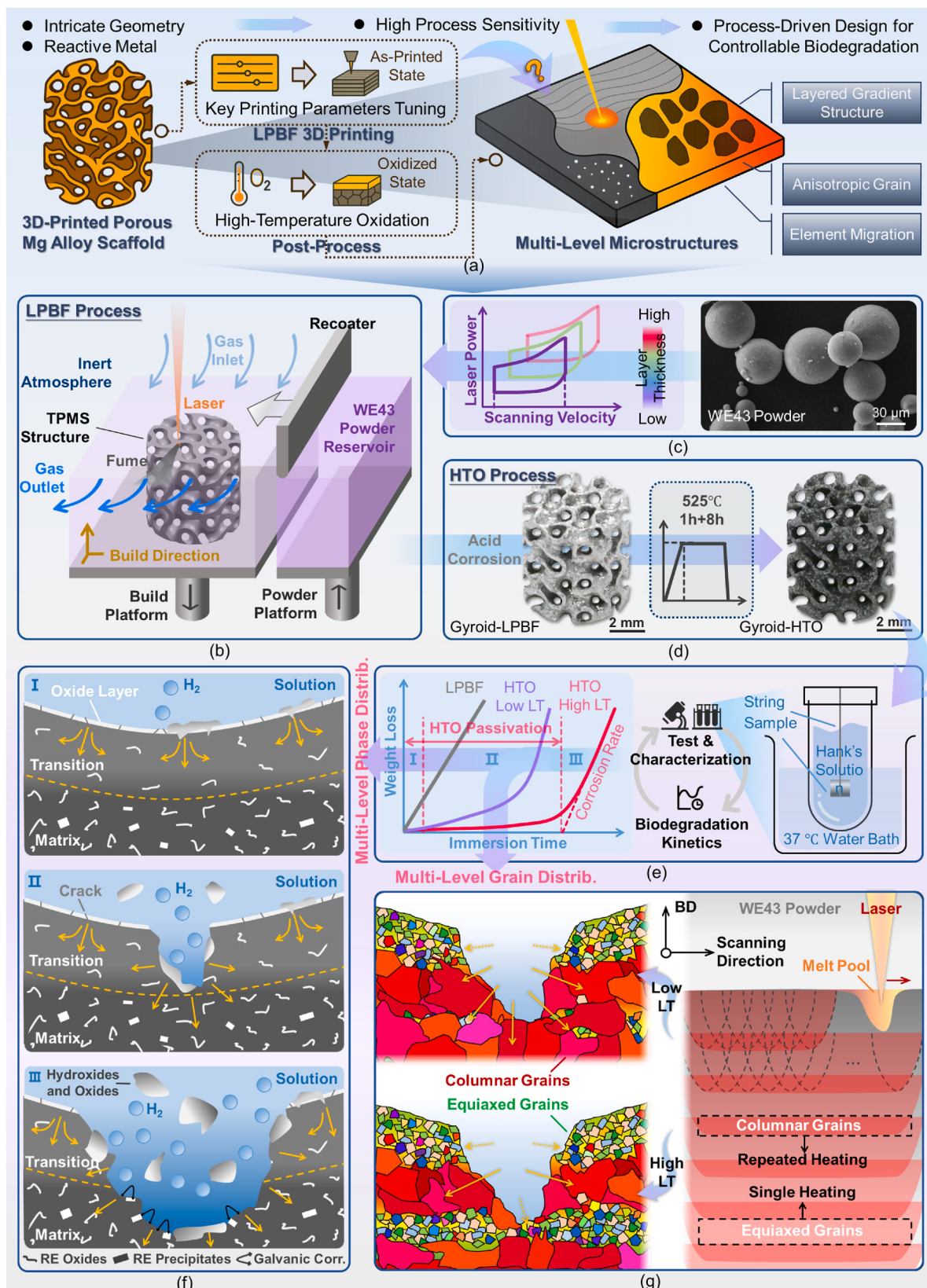


Fig. 1. Schematic diagram of the proposed work. (a) The “LPBF + HTO” hypothesis can obtain desired degradation behavior via process-driven multi-level microstructural design. (b) The LPBF process for porous WE43 scaffolds. (c) Process windows with varying laser power, scan velocity, and layer thickness, and the WE43 Mg powder used in LPBF. (d) The fabricated TPMS Gyroid structure samples before and after the high-temperature oxidation process. (e) The simulated body fluid immersion test and material characterization workflow were used to establish the degradation model. (f) The degradation mechanism of WE43 Mg alloy underlying the multi-level phase layer distribution. (g) The degradation mechanism of WE43 Mg alloy underlying the multi-level grain distribution.

(EDS). And we used the X-ray diffraction (XRD, Bruker D-8, US) to qualitatively identify various phases at the measured surfaces, where the Cu K α radiation was set at (40 kV, 200 mA) and scanned at 4°/min from 10° to 90°.

Grain Size and Texture: Electron back-scattered diffraction (EBSD, TESCAN S9000X, Czech Republic) was used to characterize the grain size, morphology, and texture of LPBF and HTO samples, using an Oxford Instruments detector operating at 20 kV with a 70° tilt angle and 0.3 μm step size. Before observation, the measured cross-sections were made parallel to the building direction and electrochemically polished with 10 vol% perchloric acid ethanol solution for 25–30 s under liquid nitrogen cooling (-40 °C). Data were analyzed using Oxford Instruments AZtecCrystal 2.1 and post-processed in Channel 5. Grain boundaries were defined using a 10° misorientation threshold, and wild spikes were removed using standard CI-based filtering.

2.4. Mechanical test

Quasi-Static Compressions: The compressive mechanical behaviors of the 3D-printed porous structures were obtained via uniaxial quasi-static compression tests, in accordance with ASTM F3122. Both φ 6 mm × 6 mm LPBF and HTO cylinder specimens were flat-compressed until densification along the building direction (z-axis), utilizing a universal testing machine (Instron 5565, UK) and an axial extensometer. The specimens were placed between two lubricated rigid platens, with the upper one moving downward at a speed of 0.5 mm/min (a strain rate of 0.001 s⁻¹ in this case). With the continuously recorded force F and displacement ΔL data, compressive engineering stress σ and compressive engineering strain ϵ were converted as

$$\sigma = F/A_0 \quad (4)$$

$$\epsilon = \Delta L/L_0 \quad (5)$$

where A_0 and L_0 represent the initial cross-sectional area and height of the cylindrical specimen, respectively, as measured by a caliper.

Determine Young's Modulus and Yield Strength: The Young's modulus E was calculated from the initial linear region (~0.1–0.3 % strain was selected) of the stress-strain ($\sigma - \epsilon$) curve using linear regression as

$$E = d\sigma/d\epsilon \quad (6)$$

The yield strength σ_y was determined using the 0.2 % offset method: draw a line parallel to the initial linear slope but offset by 0.2 % strain, and the intersection of this line with the $\sigma - \epsilon$ curve gives the yield strength. For each parameter setting, the compression test was conducted three times to report statistical variation.

2.5. Biodegradation test

Scanning Microelectrode Test: A scanning vibration electrode technique (SVET) system (Applicable Electronics Inc., USA) was applied to capture the electrochemical reactions in small, localized areas of the LPBF and HTO samples. The cross-sections parallel to the building direction were measured in Hank's solution (37 °C, pH 7.4) with a vibrating probe hanging 75 μm above the testing area (300 μm × 300 μm, 20 μm resolution). The testing area was placed within the matrix layer for HTO samples, and each condition was measured ten times.

Electrochemical Test: The electrochemical characteristics were analyzed utilizing a workstation (Metrohm Autolab, Switzerland) with a three-electrode system and NOVA 2.1 software. The system consists of a working electrode (specimen), a counter electrode (platinum), and a reference electrode (saturated calomel). In Hank's solution (37 °C, pH 7.4), the φ9.2 mm × 2 mm LPBF and HTO specimens were tested to derive the corresponding open-circuit potential (OCP) and the potentiodynamic polarization (PDP). The scan rate was 1 mV/s. The corrosion

current density I_{corr} and the polarization resistance R_p were calculated by linear fit and Tafel extrapolation at the range of ±50 mV around the corrosion potential E_{corr} . For each parameter setting, the test was conducted three times.

Immersion Test: In accordance with ASTM-G31-21, immersion tests were carried out using Hank's solution (37 °C, pH 7.4) and an exposure ratio of 20 mL/cm². Each LPBF and HTO sample was suspended in a corrosive medium with a thin wire to avoid insufficient immersion of the contact area with the container wall. The pH value variance in the solution was recorded in time sequence via a pH meter. The remaining weight of the immersion samples was measured by an electronic balance (±0.1 mg) after removing the attached degradation products using CrO₃ solution, whereas the chemical composition of the rest of the immersion solution was tested via ICP-OES after taking out the samples. Five replicate samples were tested separately for each condition. For SEM observation and photography, the LPBF and HTO samples after 1, 3, 5, 7, ..., 39 immersion days (if any) were taken out, cleaned ultrasonically in pure ethanol, and dried. The degradation products were also examined by EDS and XRD.

3. Results and discussion

3.1. Process mechanisms: Layer thickness effects on melt pool and microstructure

3.1.1. Melt pool dynamics and fusion behaviors

To explore the impact of the proposed LPBF-HTO method on microstructure evolution during metal powder melting and solidification cooling, consistent and high-quality formation was first ensured for the 3D-printed Mg alloys (Movie S1). Four key parameters were focused on: layer thickness (LT), laser power (P_L), scan speed (S_V), and preheat temperature (T_P). To ensure a sufficient relative density (ρ_s) as the primary fabrication objective, we first fixed a given layer thickness (and, where applicable, preheat temperature) and then systematically varied the laser power and scan speed. Owing to the interdependence of these parameters, this procedure allowed us to identify, for each layer thickness, a feasible process window in which ρ_s exceeded 99.0 % (see Section 2.2).

An excessively large layer thickness imposes stringent requirements on the laser power to ensure full penetration, whereas an excessively small layer thickness, for a given powder size, makes powder packing difficult and may lead to recoating failure. Therefore, we varied the printing layer thickness from 10 μm to 50 μm according to previous studies [29,33]. Four experimental groups were established for comparison, labeled LT10P, LT10, LT30, and LT50, with the feasible parameter ranges listed in Table 1.

As presented in Fig. 1d, Gyroid TPMS scaffolds were designed and fabricated at 60 % porosity and measured wall thicknesses of 400–700 μm, aligned with the practical clinical requirements for bone ingrowth, mass transport, and long-term stability [40]. Fig. 2, S1, and S2 exhibit consistent fusion quality and relative densities of the fabricated samples within the defined process windows. The variance in chemical composition before and after fabrication, attributed to metal vaporization, also indicated negligible differences (Fig. S3). From the energy point of view, these results indicate a successful identification of robust process parameter combinations for Mg alloy, where we avoided too high energy input that leads to massive evaporation, key holes, and poor dimensional accuracy, and insufficient low energy input that causes high material porosity [28]. While the linear energy input across all groups remained similar, significant variation in volumetric energy input (E_V) was observed in Fig. 2a–c, ranging from 21.0 to 119.0 J/mm³. Notably, larger LT values corresponded to lower energy input but higher surface roughness of the as-built samples (comparing Fig. 2b and d), as well as higher powder adhesion on the surface, affecting geometric accuracy and causing an unpredictable increase in surface area.

Table 1

Printing parameters setup for LPBF-HTO processes.

		LT10P	LT10	LT30	LT50
LPBF Param.	Layer thickness, LT (μm)	10	10	30	50
	Preheat temperature, T_p ($^{\circ}\text{C}$)	200	–	–	–
	Hatching space, H_s (μm)	70	–	–	–
	Laser power, P_L (W)	40–60	40–60	70–90	100–120
	Selected laser power, \bar{P}_L (W)	50	50	80	110
	Scan speed, S_V (mm/s)	500–1100	300–900	700–1300	1200–1800
	Selected scan speed, \bar{S}_V (mm/s)	800	600	1000	1500
	Volumetric energy input, E_V (J/mm ³)	77.9–114.3	95.2–190.5	33.0–47.6	19.0–23.8
	Selected volumetric input, \bar{E}_V (J/mm ³)	89.3	119.0	38.1	21.0
	Linear energy input, E_L (J/cm)	0.55–0.80	0.67–1.33	0.69–1.00	0.67–0.83
HTO Param.	Selected linear input, \bar{E}_L (J/cm)	0.625	0.833	0.800	0.733
	Heating temperature, T_H ($^{\circ}\text{C}$)	525	–	–	–
	Heating rate ($^{\circ}\text{C}/\text{mm}$)	10	–	–	–
	Holding time (hour)	8	–	–	–

Additionally, we compared the surface roughness of samples after acid polishing and after high-temperature oxidation, as illustrated in Fig. 2e–h. While thicker layers yielded more powder-adhered as-built surfaces, the surface roughness was reduced by acid polishing to a comparable low level across samples (Fig. 2e–g,h). After 525 $^{\circ}\text{C}$ heating for 8 h, the oxidation of the near-surface increased the corresponding surface roughness of HTO samples, and interestingly, the degree of impact can be related to the layer thickness again, which is elucidated in Section 3.2.

Besides, the fusion behavior of the powder bed was examined by observing the fusion line and measuring penetration depth, as shown in Fig. 3. The melt pool accumulated layer by layer along the building direction, with fusion lines identified using graphic segmentation technology (Fig. 3b). The penetration depths of the melt pool (H_p) and the uncovered deposition (H_u) that subtracts interlayer occlusion, were determined at 20 randomly selected points for each layer thickness. Varying the layer thickness affects melt pool dynamics significantly by changing both the relative penetration depth of the melt pool and its thermal stability, as further statistical analysis depicted in Fig. 3c–e and S4. It can be indicated that both penetration depths increased with a larger layer thickness (Fig. 3d). However, the scale factor, defined as H_p/LT , exhibited an inverse trend, suggesting that smaller layer thickness can result in more frequent laser remelting of the deposited metal (e.g., LT10 group undergoes estimated 40–60 times more than LT50 group). For the thickest printing layer (LT50), the melt pool depth is average three times the layer thickness, suggesting no lack-of-fusion regions. The melt pool depth was positively correlated with the layer thickness, laser power, and scan speed, yet negatively correlated with volumetric energy input. According to Eq. (1), the observed proportionality $H_p \propto P_L S_V \cdot \text{LT} / E_V$ reduces $H_p \propto S_V^2 \cdot \text{LT}^2$, indicating a dominant quadratic sensitivity to the scan speed and the layer thickness. Guided by the energy-based analysis of the key process parameters, the optimal parameter setting for each group was selected from the feasible range (Table 1).

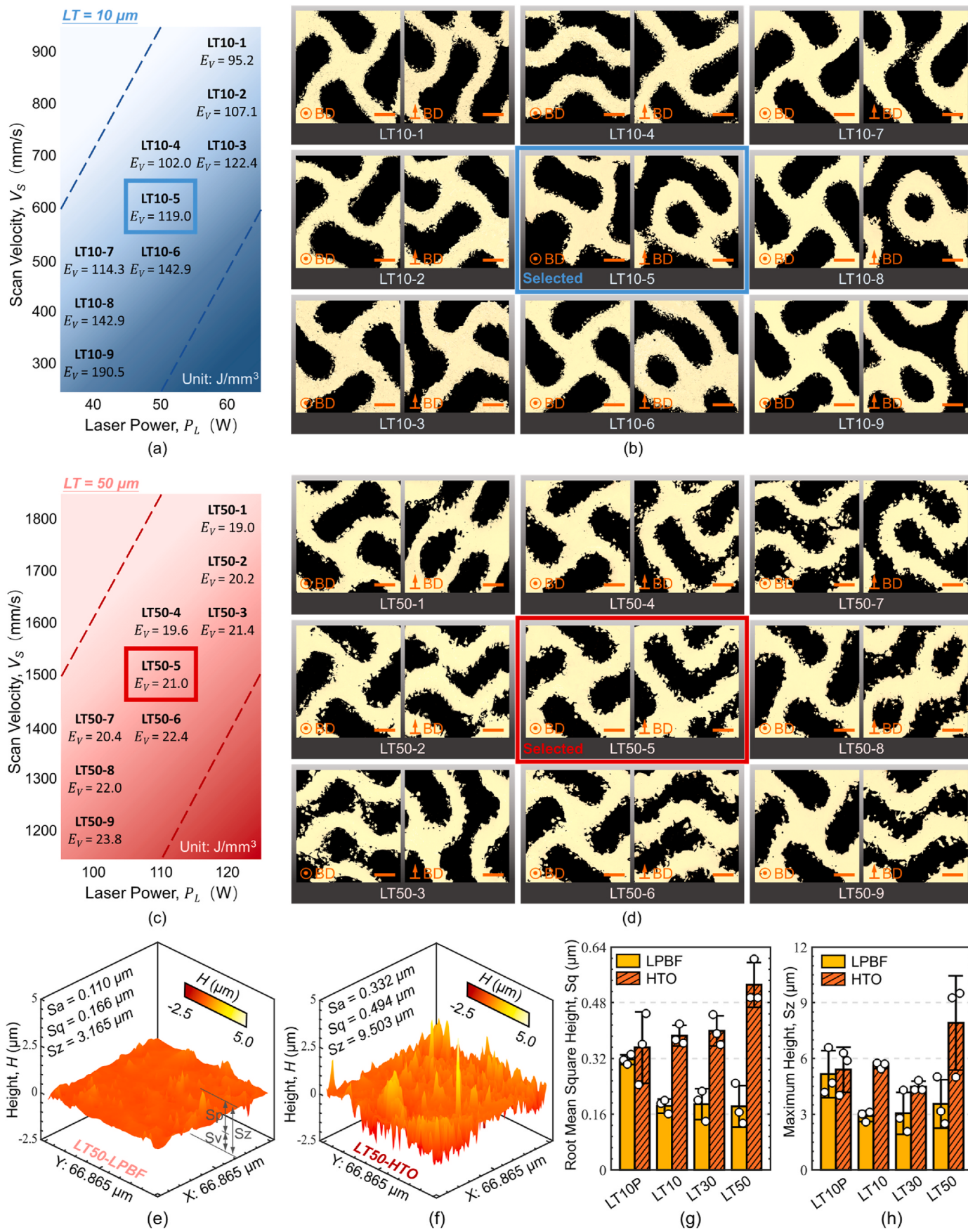
The above layer-thickness- and scan-speed-dominant correlation is embedded in the phenomenon that only specific power-speed combinations can ensure the build quality given a layer thickness. Moreover, increasing energy input led to a higher scaling factor (repetitive heating) but reduced the melt pool depth. This explains the core mechanism by which the present work controls microstructural evolution during manufacturing: tailoring the temperature gradients and thermal cycling through the choice of printing layer thickness, as shown in Fig. 3f. Specifically, a smaller layer thickness leads to smaller spatial temperature differences (along building direction) and a larger number of thermal cycles; moreover, small layer thicknesses require lower scan speeds and lower input power to ensure fusion quality, which in turn prolongs the cooling time between successive cycles. In turn, higher layer thickness causes restrained reheating times over materials yet less interlayer cooling period. For WE43, our observations have shown that,

by adjusting the layer thickness – and consequently the local energy input, thermal gradient, and solidification history – our process effectively tunes the balance between remelting and fresh solidification, which is a primary reason why different layer-thickness groups exhibit distinct solidification microstructures and subsequent corrosion behavior (see the following section). This finding highlights the ability to regulate microstructures by multiple reheating and remelting during the LPBF fabrication, especially considering the low melting and low phase-transition temperature of Mg alloys.

3.1.2. Microstructure evolution and mechanical properties

The LPBF-HTO method results in multi-level phase compositions (Fig. 4) and grain distributions (Fig. 5), enabling microstructural design in Mg scaffolds. While all samples formed similar degradation products after subsequent immersion, key microstructural differences were observed. LPBF surfaces were mainly composed of α -Mg and β 1 phases, whereas HTO samples exhibited additional MgO and rare earth (RE) oxides (Fig. 5S), confirming effective surface modification and enrichment of rare earth elements during the high-temperature oxidation process.

LPBF samples exhibit uniformly distributed secondary phases (Fig. 4a), whose matrix consistently contains α -Mg grains, residual Mg₂₄RE₅ precipitates, and rare earth oxides (primarily Y₂O₃ and Nd₂O₃) [43]. The rare earth oxides originate from the oxide shells of the chemically reactive WE43 powder particles (Fig. 1c), which form the natural passivation and remain intact due to their high melting points exceeding the peak temperature in the LPBF melt pool. These oxide shells are transformed into curved flakes due to intense laser energy exposure, as shown in Fig. 4b. On the contrary, the recrystallization and solid solution reactions during high-temperature oxidation treatment alter these uniform phase distributions. It causes a decrease in secondary phases (Fig. 4c) and the formation of scattered rare earth oxides within the matrix (Fig. 4d). SEM and EDS analysis of porous WE43 Mg scaffolds further reveals distinct gradient phases and compositional distributions in HTO samples (Fig. 4e–h and S5). These structures exhibit a well-defined layered “OL + TL + matrix” configuration: an oxidized layer at the surface, a transition layer in the intermediate region, and the WE43 Mg alloy matrix as the substrate. Within the Mg matrix, rare earth elements exhibit significant thermodynamic migration driven by oxygen partial pressure gradients, leading to selective oxidation and progressive enrichment of rare earth elements toward the surface [44]. Consequently, a near-surface region with lower rare earth content forms the transition layer (Fig. S5f). As oxygen from the ambient atmosphere diffuses inward through the growing oxide film, the oxidized layer (Y₂O₃, MgO, and Nd₂O₃) progressively forms. The oxide formation occurs through heterogeneous nucleation on the surface, which subsequently thickens and densifies, establishing a robust protective barrier, as depicted in Fig. S5a–d. It is worth noting that MgO remains the most abundant component in the oxidized layer.



(caption on next page)

Fig. 2. Fabrication quality of LPBF-HTO process. (a) Power-speed combinations at 10- μm layer thickness, with the corresponding volumetric laser energy input labeled. (b) Optical cross-sections of as-built Gyroid samples at 10- μm layer thickness, viewed along and perpendicular to the building direction (BD). The blue frame marks the parameter set selected for subsequent analyses (denoted as LT10 in the main text). Scale bar: 500 μm . (c) Power-speed combinations at 50- μm layer thickness, with the corresponding volumetric laser energy input labeled. (d) Optical cross-sections of as-built Gyroid samples at 50- μm layer thickness, viewed along and perpendicular to the building direction (BD). The red frame marks the parameter set selected for subsequent analyses (denoted as LT10 in the main text). Scale bar: 500 μm . (e) Surface morphology of LT50-LPBF samples. (f) Surface morphology of LT50-HTO samples. (g) Areal root mean square height S_q before and after high-temperature oxidation (error bars represent \pm SD from the mean value, $n = 3$). (h) Maximum height S_z before and after high-temperature oxidation (error bars represent \pm SD from the mean value, $n = 3$). (For interpretation of the references to colour in this figure legend, the reader is referred to the Web version of this article.)

To connect these process conditions to the solidification microstructure, the grain structure of the porous scaffold was also examined at the cross-section along the building direction using EBSD techniques (Section 2.3). Samples from the same LPBF batch/parameter set (e.g., LT10P, LT10, LT30, LT50) were compared pre- and post-HTO, as illustrated in Fig. 5. The grains in the fabricated Mg alloy scaffolds show significant directional alignment featuring the layer-by-layer fusion of LPBF. The average grain sizes near the upper boundary (UB) and lower boundary (DB) surfaces were measured (Fig. 5a and b) for each layer thickness group, which showed little differences with respect to the measurement regions. Grain uniformity was assessed with box plots (Fig. 5c), which show the minimum, 25th percentile (Q1), median, 75th percentile (Q3), and maximum grain sizes for each group. As seen in the grain orientation maps of Fig. 5, LPBF results in significant grain orientation along the building direction (y-direction). The microstructure comprises interleaved fine equiaxed (1–10 μm) and coarse columnar ($>50 \mu\text{m}$) grains, attributable to the repeated melting during LPBF. This anomalous grain growth and the dispersed distribution of grain sizes are particularly prominent at smaller layer thickness (Fig. 5f–i), suggesting challenges in achieving efficient grain design when input energy is relatively high. These observations are consistent with the melt pool behavior described in Section 3.1.1, where smaller layer thickness and higher volumetric energy input led to more frequent remelting.

A detailed analysis elucidates the process-induced microstructural features. HTO process modifies the near-surface layered structure and unifies the grain distribution, while LPBF parameters durably govern the post-heat-treatment phase stratification and grain-size/orientation anisotropy. Despite the consistent phase composition in the Mg matrix, as shown in Fig. 4i, the oxide layer thickness increases with higher layer thickness, correlating with the increased surface roughness observed in the HTO samples (Fig. 2e–h). It should be noted that the thickness is statistically meaningful based on multiple measurements and the EDS mapping (Fig. S5f). The transition layer is thicker in LT30 samples compared to LT10, but significantly decreases in LT50 samples, suggesting the influence of LPBF-induced grain anisotropy on the migration of rare earth elements. Meanwhile, a trend emerged where larger layer thickness led to smaller grain sizes, where LT50 has the smallest ones. The grain refinement trend observed here is consistent with the findings in our earlier study on LPBF WE43 alloy bulk [33]. Although preheat reduces thermal gradient during laser processing, leading to lower residual stresses, it can slow down the cooling rate, which promotes coarser grains (referring to Fig. 5d). As layer thickness increases, the volumetric energy input and the number of repeated heating cycles decrease, leading to more equiaxial crystals and smaller average grain sizes. Interestingly, after HTO treatment, the grains recrystallize, leading to moderate grain growth and uniform grain distribution, while the anisotropic grain texture induced by LPBF is maintained.

Specifically, the LT50-HTO samples exhibit the finest grain texture near the surface (Fig. 5n), which provides a high density of grain boundaries. These grain boundaries serve as fast diffusion paths for oxygen and RE elements during high-temperature oxidation [45], promoting non-uniform oxide growth and localized swelling of the oxide scale. Therefore, the oxidized layer in the LT50-HTO group is thick but less dense, and the root mean square height and the maximum height are

sharply elevated, suggesting 50 μm is an inappropriate layer thickness for porous WE43 alloy scaffolds. Among the four groups, LT30 exhibits the least HTO-induced increase in roughness and the tightest grain-size distribution (Fig. 5c–l), evidencing a relatively more homogeneous microstructure arising from the LPBF-HTO synergy.

Furthermore, quasi-static compression tests were performed along the axial direction (i.e., the building direction) on the scaffold samples to characterize the microstructural difference, as shown in Fig. 6a–d. The corresponding Young's modulus E and the yield strength σ_y were derived referring to Section 2.4. The variation of these indicators, as well as the ductility of WE43 scaffolds, confirmed the significant roles of process-driven microstructure, which is an integrated impact of grain size and texture. Referring to Fig. 6e, the modulus and the strength of the LPBF samples decreased with increasing layer thickness. Though refined grains were observed by increasing layer thickness (Fig. 5), the highly anisotropic columnar crystal and strong crystallographic textures attributed to thinner layers caused direction-dependent mechanical properties in porous structures, which explains the enhancement of stiffness and strength along building direction in the LT10-LPBF samples. For the LT10P-LPBF samples, the preheating further increased the grain orientation along the building direction and resulted in the highest stiffness and strength among test conditions. Moreover, given the same porosity (60 %), the LPBF samples have higher modulus and yield strength than the HTO samples. The LPBF samples gradually collapsed into disjointed fragments during compression, and the brittleness was indicated by the undulating yield plateau on the stress-strain curves (Fig. 6a–d). On the contrary, the ductility of the structure after HTO was improved with a significant decrease in the first peak force and a long and uniform yield plateau, even though oxide coating on Mg alloy can reduce ductility due to easy-to-crack brittle oxide scales [46]. This indirectly corroborates that the HTO-induced oxidized layer was dense and continuous. High-temperature oxidation treatment was in favor of grain growth, and made the grains more uniform and less oriented (Fig. 5), thus reducing strength yet improving ductility. While the mechanical responses within LPBF groups differed, HTO groups showed more consistent performance among different process conditions. Such changes from LPBF to LPBF-HTO underscore the dominant mechanical effect of the heat treatment post-process through microstructure modulation, which can even out the difference brought by the LPBF process. It is worth pointing out that, with a need to match the deformation of surrounding bone, the increased ductility and stability of Mg alloy scaffold contributed from the microstructure evolution of HTO fit the biomechanical functionality required from bone implants [47].

3.2. Enhanced biodegradation resistance via LPBF-HTO process

3.2.1. Degradation resistance by electrochemical tests

The degradation resistance of LPBF-HTO-processed Mg alloy scaffolds was evaluated by examining both the global and localized electrochemical properties in a simulated body fluid (SBF) environment. First, a $300 \times 300 \mu\text{m}^2$ region at the center of the longitudinal cross-section (Fig. 5a) was selected for SVET to probe matrix microstructural influence, based on the high-resolution measurements of localized corrosion activity (e.g., current variations) in the microscale. Fig. 7 presents the corrosion current density (i_{corr}) distributions in the scanned regions, and the uniformity of electrochemical response is quantified

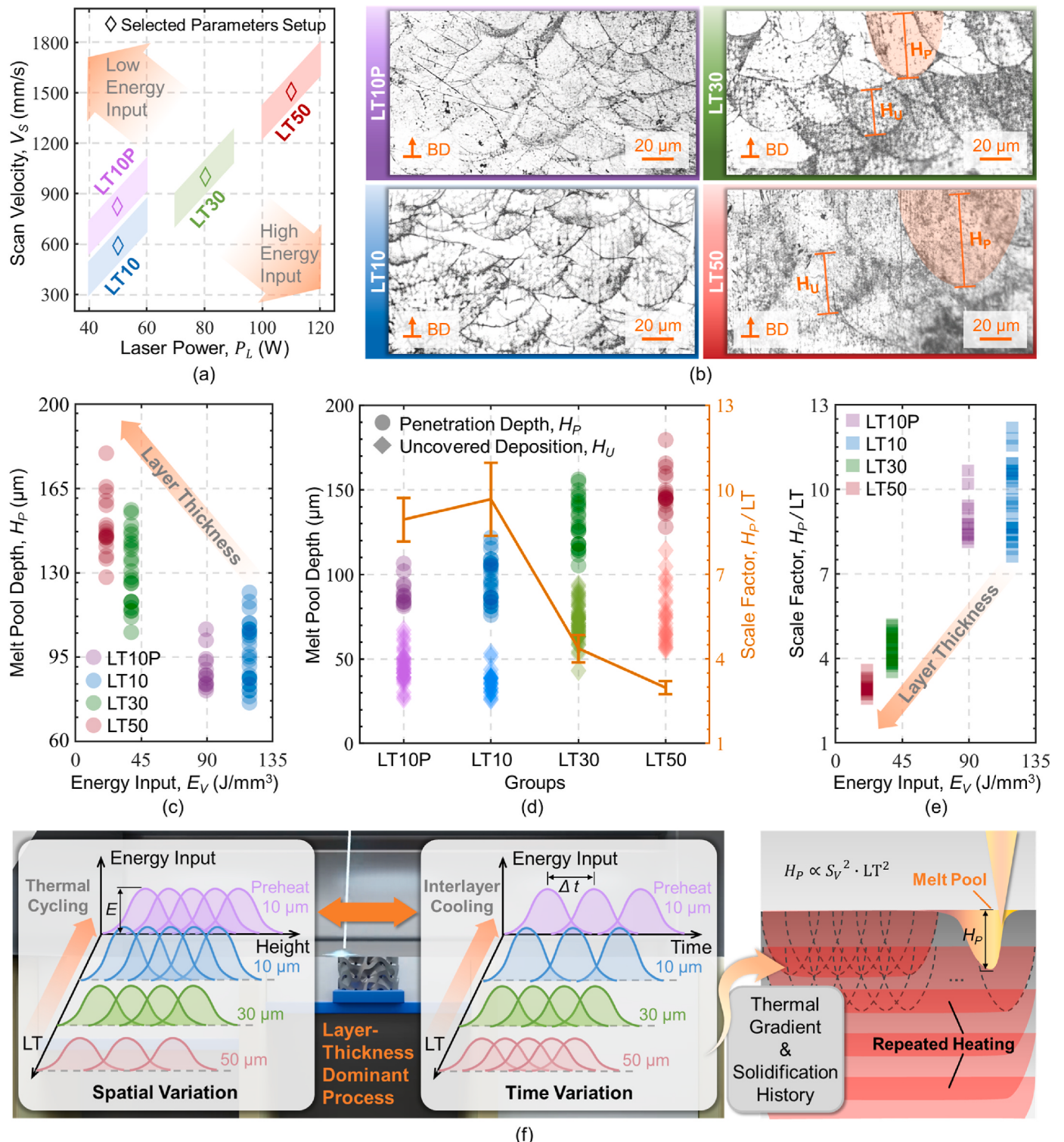


Fig. 3. Parameters and fusion behavior of LPBF-HTO process. (a) Process window of LPBF showing variations in laser power and scan velocity. (b) Optical images showing fusion lines in the LT10P, LT10, LT30, and LT50 group, with the penetration depth H_p and the uncovered deposition H_u marked. (c) Correlation between the melt pool penetration depth H_p and the volumetric energy input E_V . (d) Scattering plot of the melt pool penetration depth for various groups, with the scaling factor variance indicated by the orange line (error bars represent \pm SD from the mean value, $n = 20$). (e) Correlation between the scale factor H_p/LT and the volumetric energy input E_V . (f) Layer-thickness-dominant process mechanism that causes spatial and time variations for melt pool dynamics to regulate thermal gradient and solidification history, which reveals a quadratic proportion with layer thickness to penetration depths of melt pool. (For interpretation of the references to colour in this figure legend, the reader is referred to the Web version of this article.)

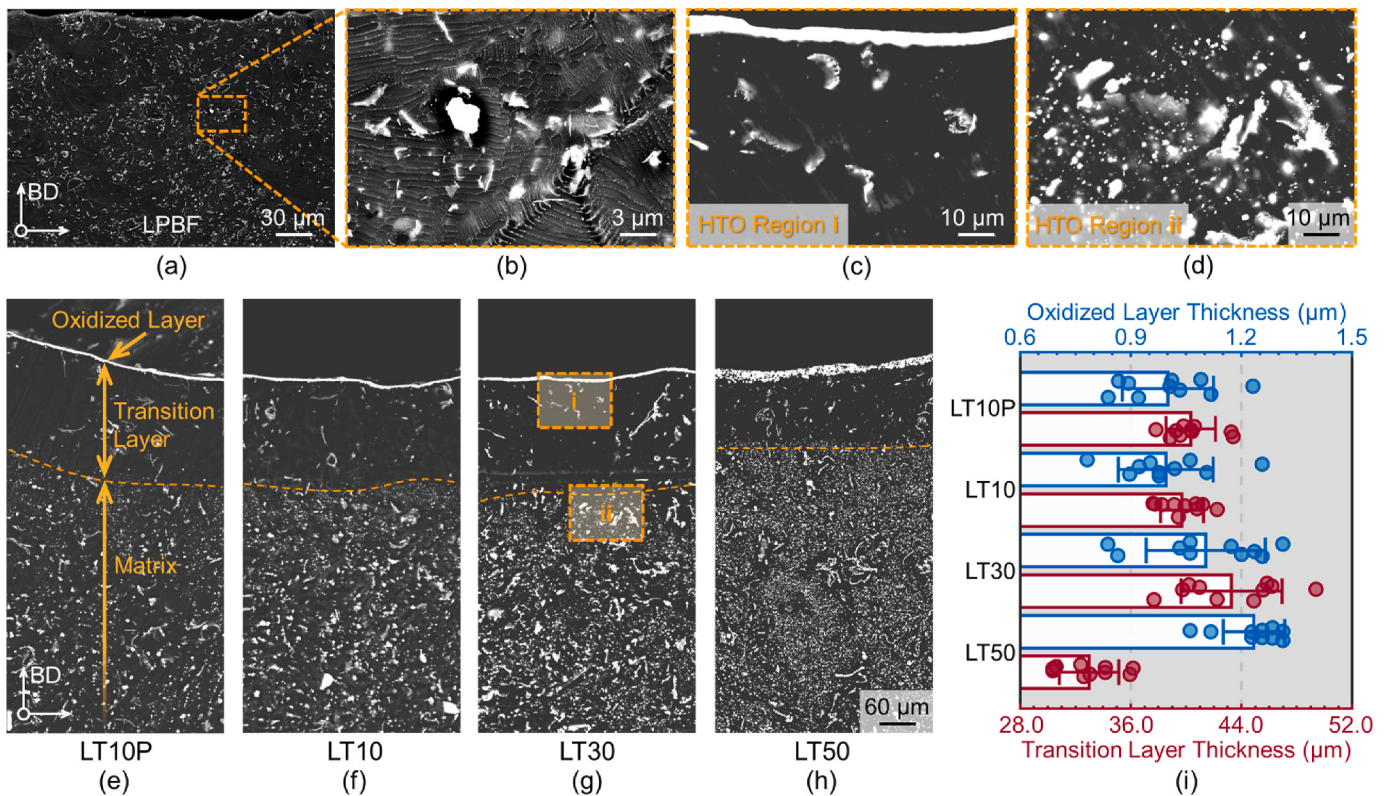


Fig. 4. SEM characterization of microstructures during LPBF-HTO process. (a) Cross-sectional SEM images of the near-surface regions of LPBF samples. (b) High-magnification view of the matrix in LPBF samples. (c) Magnification view of region-i in HTO samples, featuring an oxidized layer and a transition layer. (d) Magnification view of region-ii in HTO samples, featuring the boundary between the matrix and the transition layer. Cross-sectional SEM images of the near-surface regions of (e) LT10P, (f) LT10, (g) LT30, and (h) LT50 HTO-treated samples. (i) Bar plots showing the thickness of the oxidized layer and the transition layer across different layer thickness groups. Circular points represent raw data values; error bars represent \pm SD from the mean value ($n = 10$).

using the root mean square (RMS) values of i_{corr} . Attributed to the disordered grain size and morphology, LPBF samples exhibited elevated and highly variable corrosion current density, reflecting active hydrogen gas evolution and high degradation tendency. In contrast, HTO-treated samples showed significantly reduced and more uniform corrosion activity. The absolute current densities were not only smaller but also more evenly distributed, with RMS i_{corr} reduced by one to two orders of magnitude compared to their LPBF counterparts. Importantly, these results pertain to the matrix alone and thus exclude surface passivation by the oxide layer. With micron-scale contour resolution capturing microstructural variation along the build direction (Fig. 7a–h), the local current fluctuations reflect representative matrix electrochemistry. Among all groups, the LT30 samples displayed the most homogeneous electrochemical behavior in both LPBF and HTO states, aligning well with the uniform grain size distribution previously observed in Fig. 5. This suggests a strong correlation between microstructural uniformity and electrochemical stability.

To evaluate global biodegradation behavior, potentiodynamic polarization (PDP) tests were performed using $\phi 9.2\text{ mm} \times 2\text{ mm}$ porous discs (Fig. 7j). HTO-treated samples consistently demonstrated more positive corrosion potentials compared to LPBF samples, indicating enhanced resistance to electrochemical corrosion. Fig. 7k shows that high-temperature oxidation treatment markedly improves corrosion resistance – corrosion current densities (I_{corr}) decrease and the corresponding polarization resistance (R_{corr}) increases, typically by > 1 order of magnitude. Notably, the LT30 group again performs best, with the lowest I_{corr} and highest R_{corr} . This stems from its more uniform grain structure, which promotes a more stable oxide layer (Fig. 4) and stronger passivation. Among the tested conditions, 30 μm layer thickness combined with LPBF-HTO yields the most corrosion-resistant microstructure.

3.2.2. Degradation behavior in static corrosion

The biodegradation of porous WE43 Mg alloy scaffolds is fundamentally a composition-structure-environment controlled corrosion process that occurs within the implantation site, which is dominated by the LPBF-HTO-introduced microstructure. As shown in Fig. 8a, the porous structures were cross-sectioned along the build direction to directly expose the matrix and the transition layers to Hank's solution at 37 °C for 1 h. The LPBF samples corroded pervasively and degraded uncontrollably with loosely attached precipitate. By contrast, the HTO samples showed minimal reaction in the matrix, while limited localized corrosion appeared in the transition layer just beneath the oxide, forming faint Mg hydroxide deposits. The sparse reaction sites in HTO samples were difficult to detect by SEM, indicating a delayed onset of degradation. As seen in Fig. 8b, calcium-phosphorus (Ca-P) compounds gradually accumulated on the oxide surfaces of HTO samples, while the underlying Mg began eroding from the exposed edges inward. These Ca-P precipitates, primarily hydroxyapatite (HA) and tricalcium phosphate (β -TCP), contributed to surface passivation and slowed the degradation process.

Compared with the matrix, the deteriorated corrosion resistance of the transition layer can be attributed to the compositional and microstructural migration during the high-temperature oxidation treatment. On one hand, the rare earth elements migrated to the surface and form the oxide layer, resulting in a reduction of the passivation effect in the transition layer compared to the matrix. On the other hand, rare earth oxides, particularly yttrium oxide, acted as corrosion barriers. Their presence, confirmed by Figs. 4 and 8c, was more prominent in the matrix layer, helping it resist corrosion more effectively than the transition layer. X-ray diffraction (XRD) analysis further supported these observations (Fig. 8d and S6).

Besides the cross-sectional immersion test, the degradation of the

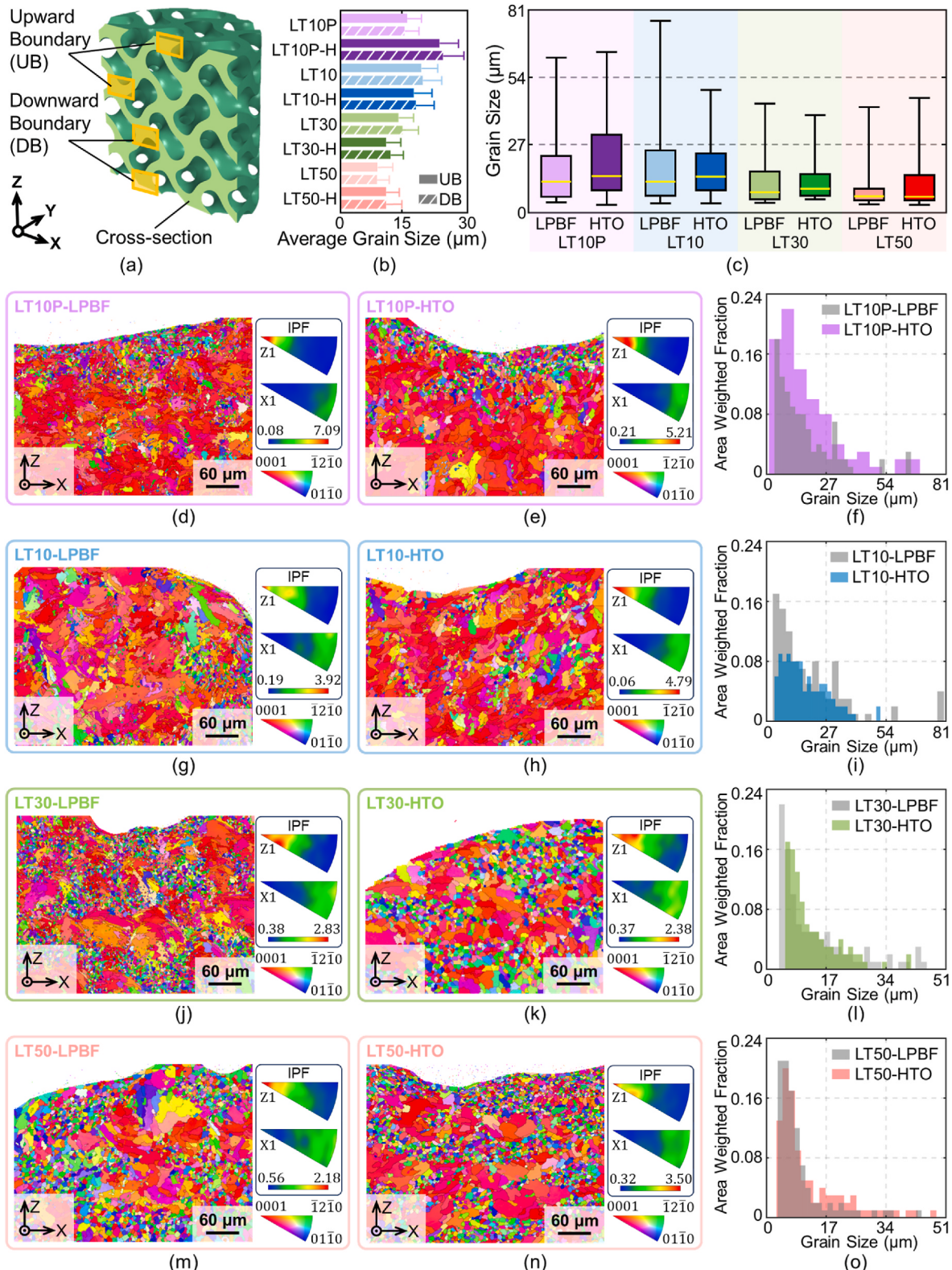


Fig. 5. Grain characterization of LPBF-HTO Mg alloy scaffolds. (a) Cross-sectional observation in the upper boundary (UB) and lower boundary (DB) regions of the samples. (b) Average grain sizes across different sample groups. The high-temperature oxidation is denoted with the suffix “H,” while the LPBF-only state is shown without a suffix. Error bars represent \pm SD from the mean value ($n = 3$). (c) Box plots of grain size distributions for each group, indicating the maximum, 25 %, 50 %, 75 %, and minimum values. (d) Grain orientations, grain boundaries, and inverse pole figures of LT10P-LPBF samples. (e) Grain orientations, grain boundaries, and inverse pole figures of LT10P-HTO samples. (f) The grain size distribution of the LT10P groups was measured by equivalent circular diameter. (g) EBSD results of LT10-LPBF samples. (h) EBSD results of LT10-HTO samples. (i) Grain size distribution of LT10 groups. (j) EBSD results of LT30-LPBF samples. (k) EBSD results of LT30-HTO samples. (l) Grain size distribution of LT30 groups. (m) EBSD results of LT50-LPBF samples. (n) EBSD results of LT50-HTO samples. (o) Grain size distribution of LT50 groups.

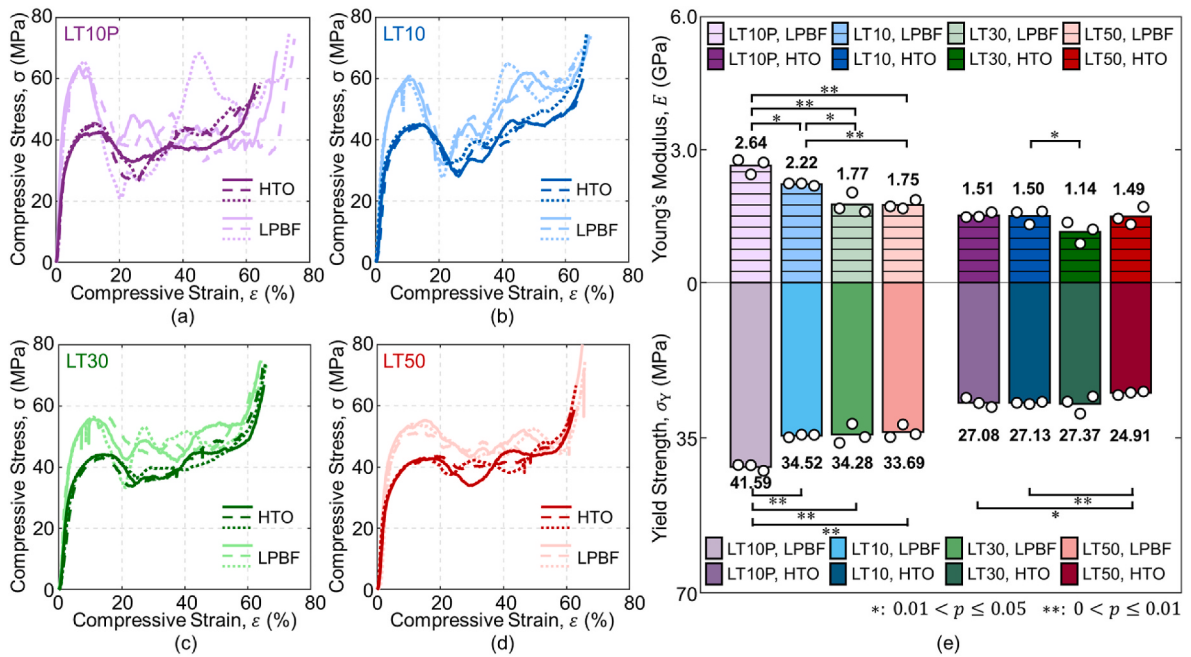


Fig. 6. Mechanical properties of the LPBF-HTO porous Mg alloy scaffolds. The quasi-static compression stress-strain curves of (a) LT10P, (b) LT10, (c) LT30, and (d) LT50, respectively. The LPBF and HTO samples of each group were compressed until crushed with respective three duplicate tests. (e) Mean value of Young's modulus and yield strength with different process conditions and layer thickness settings. The results comprise the original data accompanied by the p-value ($n = 3$).

intact WE43 scaffolds further emphasized the importance of process-driven microstructural features, as depicted in Fig. 8e,f, and S7. It was revealed that, during the first week of immersion, high-temperature oxidized samples developed initial Ca-P “brick-like” deposits that gradually expanded. With deeper corrosion activity over time, a secondary layer of porous, grayish-white precipitates formed. However, RE oxides within the matrix slowed the inward progression of corrosion, and HTO samples generally experienced less structural damage than their LPBF counterparts, which have lower oxide content.

The total degradation duration varied significantly with process settings, as the macroscopic degradation morphology of the scaffolds with respect to immersion time shown in Fig. 9. LT10-HTO degraded almost completely within one week, and LT10P has the highest degradation rates, which is primarily attributed to the coarse and anisotropic columnar grains. Preheating in LPBF proved disadvantageous for degradation, outweighing its putative benefits. In contrast, the LT30-HTO group retained approximately 43 % of its original mass after 28 days of immersion. And it showed the greatest resistance, remaining structurally intact for up to an average of 39 days. Moreover, high-temperature oxidation treatment improved the biodegradation resistance of the LT10 and LT30 groups by around 50 % and 31 %, respectively, compared to their LPBF counterparts. This improvement is comparable with PEO-treated porous structures [48]. The order regarding degradation rates from highest to lowest was approximately: LT10P > LT50 ≈ LT10 > LT30. Notably, these similar rates of LT10 and LT50 groups arose from distinct microstructural factors: matrix corrosion in LT10 was driven by its coarse-grain structure and associated anisotropic corrosion pathways, whereas in LT50 it resulted from the insufficient protection provided by the porous oxide scale. Although LT50 exhibited a finer and more uniform mixed grain structure compared to LT10 (Fig. 5), its biodegradation resistance was undermined by the formation of a thicker but porous and poorly adherent oxide layer (Fig. 4h). This layer failed to provide effective passivation and allowed an early penetration of corrosive species and matrix exposure, which indicates that the density rather than the thickness of the oxide layer plays a crucial role in delaying degradation.

It is worthwhile to mention that in LT10P and LT50 groups, the high-

temperature oxidized samples can have inferior biodegradation performance even compared to their corresponding LPBF states. As demonstrated in Fig. 8, the oxidized layer in the HTO samples initially suppresses corrosion, aided by surface Ca-P deposition. However, degradation of the transition layer can begin as early as Day 1, indicating that the overall protection at this stage heavily depends on the surface's passivation capability. Rougher surfaces (Fig. 2g and h) elevate pit/crevice initiation and impair adherence of protective products, undermining the barrier. Once corrosion extends beyond the surface, microstructure dominates, where coarse/columnar and anisotropic grains facilitate localized attack and rapid propagation. Together, these observations explain when high-temperature oxidation underperforms: as-printed roughness/defects and grain anisotropy bias oxide nonuniformity and early breach, negating the expected benefit – most noticeably in LT10P and LT50 groups. It elucidates that the HTO process is effective only when the LPBF-induced state supports uniform passivation, i.e., low roughness, minimal defects, and near-isotropic fine grains.

LT30 group exhibited the most favorable grain characteristics – a combination of fine equiaxed grains near the surface and columnar grains in the underlying layers – which provided an optimal balance between grain boundary density and crystallographic orientation via texture control [49]. This configuration reduced fast diffusion pathways for corrosive species and promoted the formation of a dense, adherent oxide scale during high-temperature oxidation, resulting in enhanced passivation and superior biodegradation resistance. This mixed grain structure contributed to micro-regional electrochemical stability by minimizing localized corrosion initiation sites while supporting uniform degradation progression. Corroborated by both micro- and macro-scale corrosion tests, the observed degradation trends and weight loss profiles for LT30 reflect this mechanism, where both grain and oxide layer work synergistically to slow biodegradation.

The integrated regulation of degradation resistance through multi-level microstructural design was further validated by kinetic analyses. In addition to the weight loss data presented in Fig. 9b, biodegradation was evaluated through pH changes and ion release profiles, as shown in Fig. 10. These variables closely mirrored the observed degradation rates and helped reveal the underlying corrosion dynamics. Greater

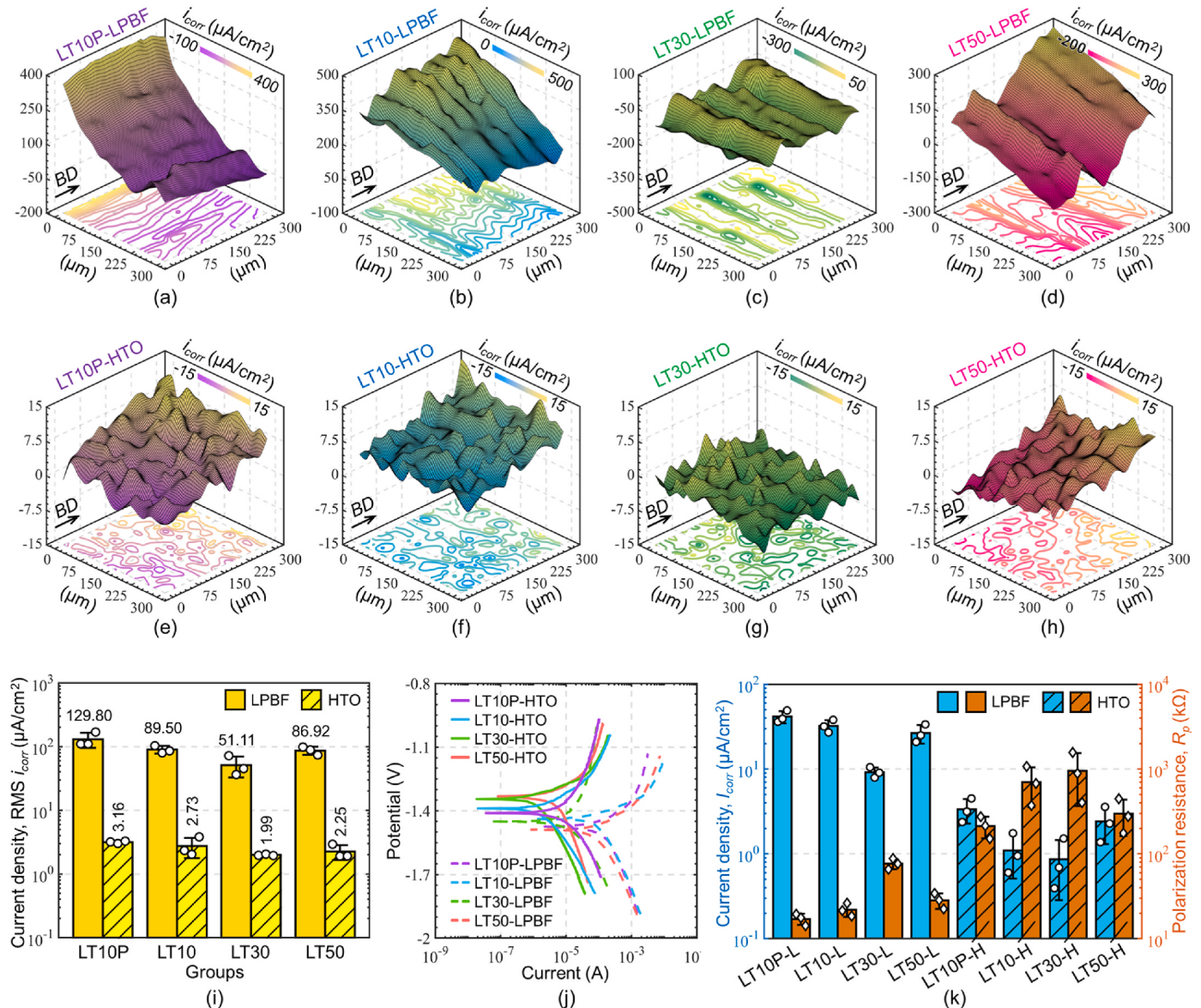


Fig. 7. Electrochemical testing of LPBF-HTO WE43 scaffolds. Corrosion current density i_{corr} contour map ($300 \times 300 \mu\text{m}^2$) for (a) LT10P-LPBF samples, (b) LT10-LPBF samples, (c) LT30-LPBF samples, (d) LT50-LPBF samples, (e) LT10P-HTO samples, (f) LT10-HTO samples, (g) LT30-HTO samples, and (h) LT50-HTO samples. (i) Root mean square (RMS) values of i_{corr} for each layer thickness group, indicating the uniformity of local electrochemical behavior. Error bars represent $\pm \text{SD}$ from the mean value ($n = 3$). (j) PDP curves for LPBF and HTO samples across all layer thickness groups. (k) Macro-scale corrosion current density I_{corr} and polarization resistance R_p of WE43 Mg scaffolds under different processing conditions. Error bars represent $\pm \text{SD}$ from the mean value ($n = 3$).

dispersion was observed in the HTO groups relative to LPBF; even so, the kinetic behavior proved robust and reproducible across replicates. During immersion, Mg ions and hydrogen were gradually released into the surrounding fluid, accompanied by a rise in pH, as shown in Fig. 10a–h. Due to the consistent initial mass of the samples, ion concentrations and pH values showed minimal differences across groups once the structures collapsed. These values stabilized within the range of 0.6–1.0 g/L for Mg ions and pH 10.2–10.6. However, the early degradation phase (Days 1–7) revealed notable differences. HTO-treated samples exhibited a slower rise in both Mg ion concentration and pH, reflecting an effective surface passivation. Specifically, LT30-HTO showed the slowest pH increase (Fig. 10c) and the lowest Mg ion release by Day 28 (Fig. 10g), aligning with its delayed degradation observed in prior results.

A deeper look into ion concentration changes in the LT30 group (Fig. 10i and j) revealed further insights into the influence of process-driven microstructure on the degradation mechanism. The release of

both Mg and RE ions in HTO samples was, to a notable extent, lower than that in LPBF samples throughout the degradation cycle. During the initial immersion stage, where the oxidized and transition layers were the primary degradation sites, the ion release rate in HTO samples was 3–7 times slower, indicating effective corrosion suppression. Even in later stages, HTO samples continued to outperform their LPBF counterparts in terms of resistance, demonstrating the long-term benefits of the designed multi-level microstructure. An additional indicator of degradation dynamics was the Mg-to-RE ion ratio. As shown in Fig. 10j, LPBF samples maintained a relatively constant ratio matching their solid-state composition (per Fig. S4) throughout degradation. In contrast, HTO samples exhibited a temporarily elevated Mg-to-RE ratio in the first two weeks before stabilizing, suggesting that early degradation primarily occurred in the transition layer where RE elements were less concentrated due to prior redistribution. This observation reinforces the understanding that microstructural layering not only delays degradation but also directs its progression. Finally, the marked

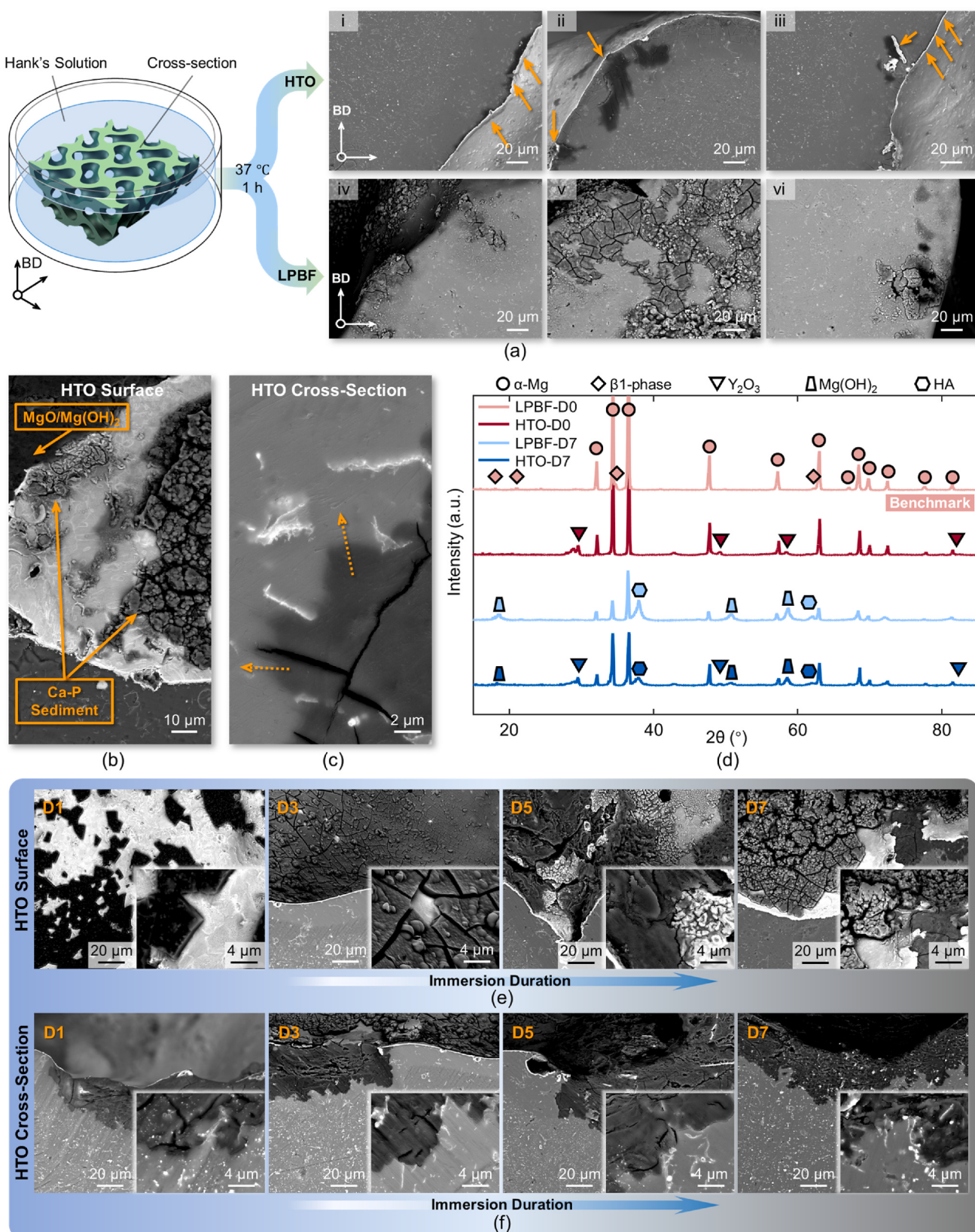


Fig. 8. Degradation mechanism and immersion progression of 3D-printed WE43 scaffolds. (a) Cross-sectional immersion test, with the 1-h corrosion behavior shown in i-iii and iv-vi for the HTO and LPBF samples, respectively. (b) Surface of HTO samples in degradation. (c) Cross-section of HTO samples in degradation. (d) XRD analysis of surface composition for LPBF and HTO samples before (Day 0) and after immersion (Day 7). Note that phases already identified in the "LPBF-D0" pattern (as benchmark) are not repeatedly labeled in the lower curves to avoid overcrowding, although they are also present there. (e) Corrosion morphology of the surface of HTO samples from Day 1 to Day 7. (f) Corrosion morphology of the cross-section of HTO samples from Day 1 to Day 7.

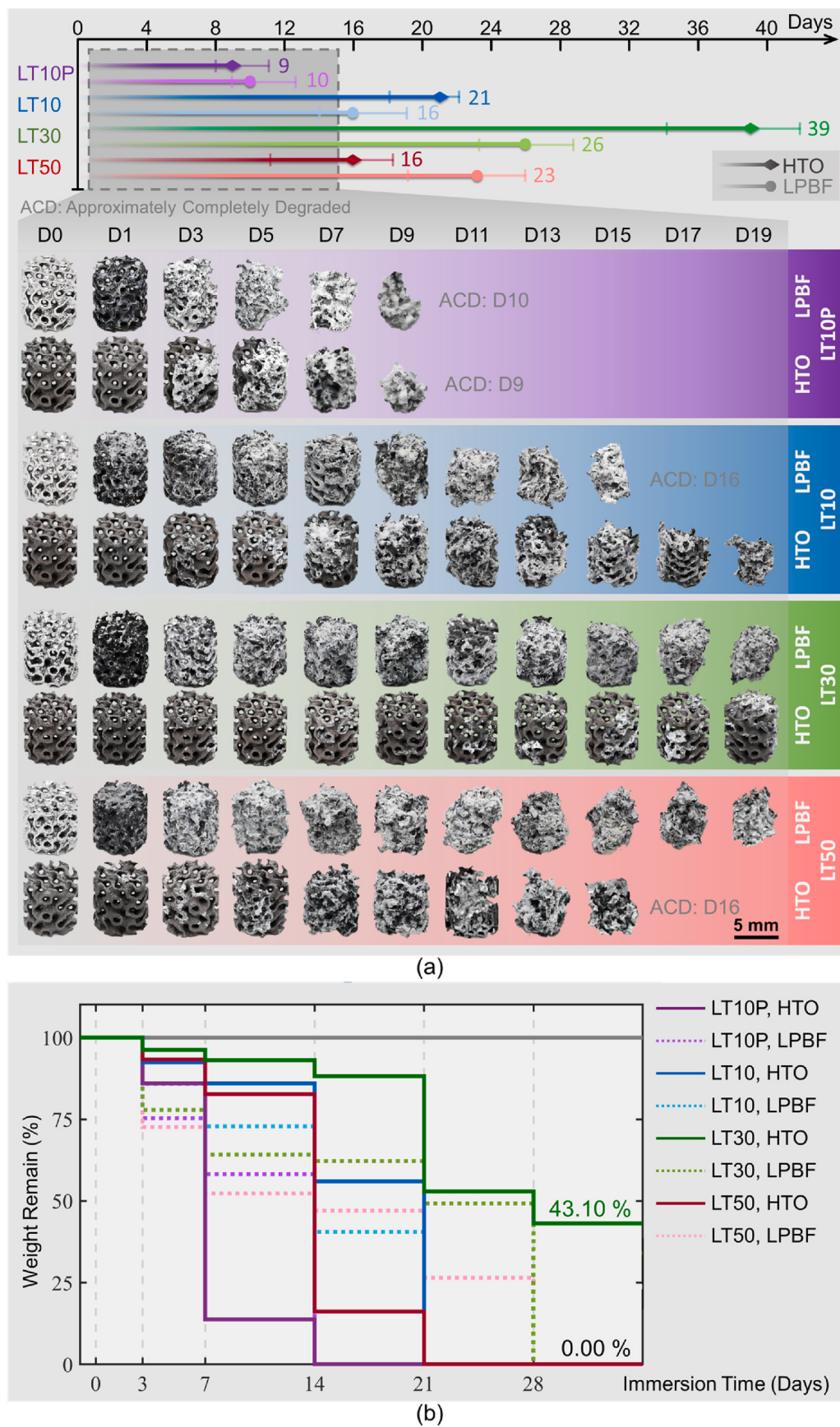


Fig. 9. Degradation progression of porous Mg alloy scaffolds. (a) Complete degradation cycles of samples with different LPBF/HTO states and layer thickness (LT) settings, indicating the time to approximately complete degradation (ACD). Mean shown; error bars span min–max ($n = 5$). (b) Residual weight percentage of each group over 28 days of immersion.

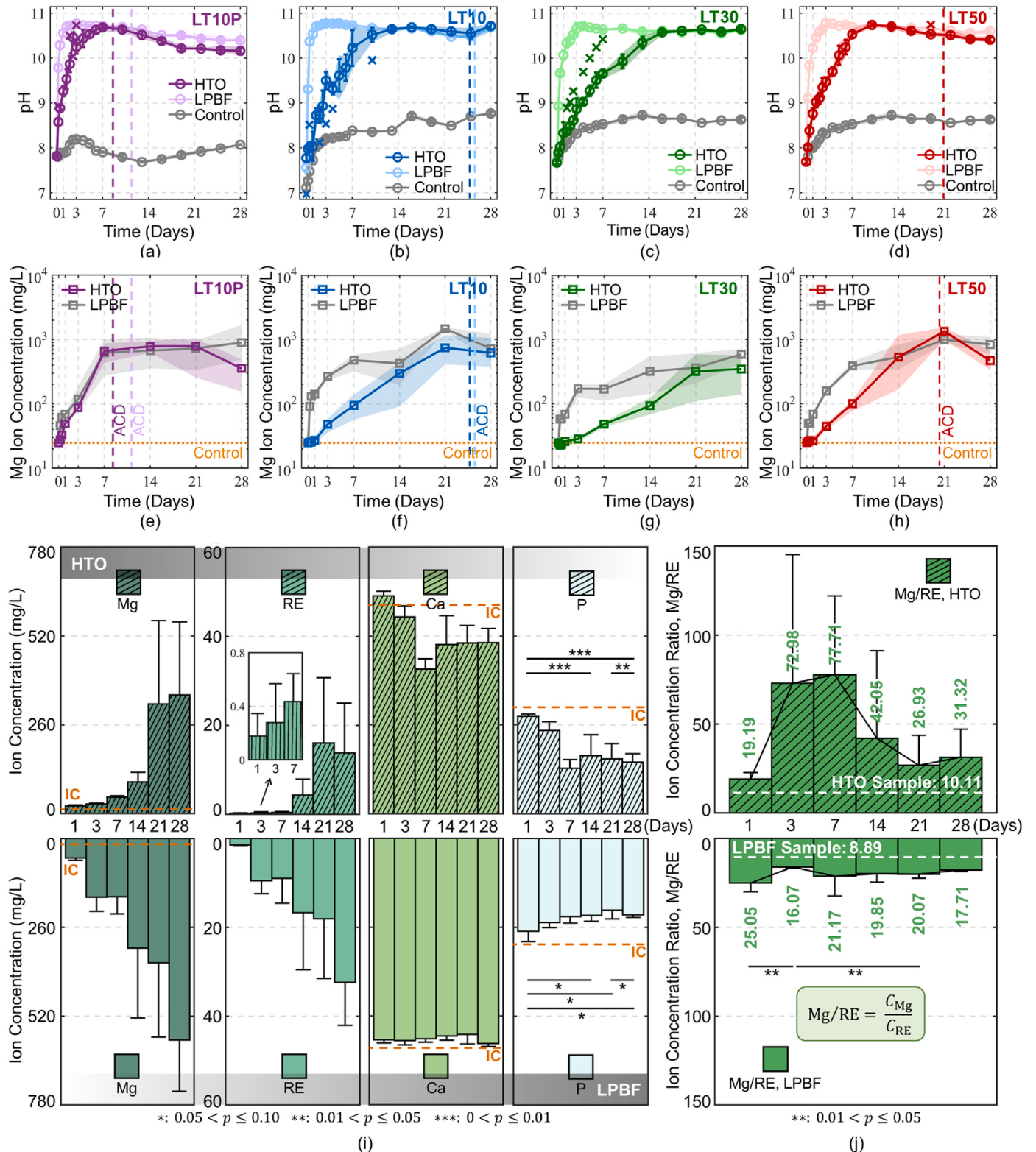


Fig. 10. Biodegradation kinetics of 3D-printed WE43 scaffolds. pH variations over immersion time for (a) LT10P, (b) LT10, (c) LT30, and (d) LT50 samples, respectively. Outliers are marked with crosses, determined using the 3σ criterion. Mg²⁺ ion concentration profiles over time for (e) LT10P, (f) LT10, (g) LT30, and (h) LT50 samples, respectively. Vertical dashed lines represent the corresponding approximate complete degradation (ACD) times. (i) Time-dependent ion release profiles for the LT30 group with respect to Mg, RE, Ca, and P elements, respectively, from left to right (IC: initial concentration in Hank's solution). (j) The Mg-to-RE mass concentration ratio released by WE43 scaffolds. Error bars represent \pm SD from the mean value ($n = 5$); p-value is annotated.

concentration decreases in Ca and P ions in HTO samples pointed to the formation and deposition of calcium-phosphate (Ca-P) compounds, which contributed to surface passivation and further slowed degradation.

Remarkably, the degradation cycles (Fig. 9a) and the kinetic trajectories (Fig. 10) closely track the grain-size distributions (Fig. 5c), mutually corroborating the microstructure-degradation linkage. The morphology of the corroded structures and the corresponding weight loss data also reflect distinct degradation patterns: LPBF samples, without surface modification, exhibited a more homogeneous and “linear” mode degradation profile; in contrast, high-temperature oxidized samples displayed a “nonlinear” degradation process. Specifically, during the early stage (Days 1–7), degradation was minimal and limited primarily to the oxide and transition layers, with little accumulation of surface degradation products. In the mid-stage (Days 7–14), degradation intensified as the matrix layer became the primary site of corrosion, marking a transition to a more aggressive degrading stage. The established degradation model is illustrated in Fig. 1e and Movie S2. We also performed index-based quantification to directly link process parameters, microstructural descriptors, degradation kinetics, and mechanical performance, as shown in Fig. S8. These findings show that process-driven microstructural design via controlled LPBF–HTO provides a practical route to control biodegradation kinetics in porous Mg scaffolds. The ability to tailor grain size, grain morphology, and oxide layer characteristics offers clear guidance for designing structures with targeted biodegradation performance [40].

4. Conclusions

The rapid biodegradation of 3D-printed porous Mg alloys poses a significant challenge for bone implant applications. This study addresses this limitation by tailoring the corrosion-resistant microstructural features after high-temperature oxidation heat treatment through the control of key processing parameters. A multi-level distribution of microstructure is effectively achieved, which comprises elemental (rare earth) concentration gradients, grain-size/orientation anisotropy, and dense oxide layers. By clarifying the relationship between the LPBF layer thickness and the degradation performance, this study elucidates the decisive role of the multi-level microstructures in governing the biodegradation kinetics of porous Mg alloy scaffolds.

- 1) **Adjusting the layer thickness in LPBF is an effective and robust approach to modulate the grain anisotropy and size distribution within porous Mg scaffolds (Figs. 2, 3, 5 and 6).** The low melting point and high reactivity of Mg make its microstructural evolution highly sensitive to energy input and thermal fluctuations induced by processing parameters and conditions. Such sensitivity is further amplified when printing porous scaffolds with thin walls and varying curvature, leading to pronounced differences in grain state and ultimately resulting in differentiated compressive properties and corrosion tendencies. At higher layer thicknesses (e.g., 30 and 50 μm), the reduced volumetric energy density required to ensure build quality, together with fewer thermal cycles, promotes the dominance of equiaxed grains, which become finer and more uniform in size (diameter 0.5–2 μm). In contrast, at lower layer thicknesses (e.g., 10 μm), strongly oriented columnar grains prevail. Moreover, preheating the substrate to 200 °C reduces the thermal gradient but paradoxically intensifies anisotropy and abnormal grain coarsening (diameter 5–20 μm).
- 2) **High-temperature oxidation induces a stratified passivation structure through elemental migration while inheriting the grain characteristics resulting from 3D printing (Figs. 2, 4 and 8).** During oxidation, rare-earth elements diffuse toward the surface, where they combine with atmospheric oxygen to form a ~1–2 μm oxidized layer (OL). The density and integrity of the oxide layer are further influenced by the surface roughness of the 3D-printed part,

which was related to the printing parameters. Owing to the limited penetration depth of elemental migration, a near-surface transition layer (TL) with reduced rare earth and oxygen content develops between the superficial oxide layer and the underlying matrix. Such “OL + TL + matrix” layered structure plays a pivotal role in regulating the degradation rate. Meanwhile, recrystallization and coarsening of the Mg matrix, accompanied by the solid-solution behavior of rare-earth elements, alter the phase layer distribution but largely retain the grain features established during the printing process.

- 3) **Guaranteeing a well-fabricated scaffold with process-induced multi-level microstructure is the primary driver of controlling degradation behavior (Figs. 7, 9 and 10).** The LT30-HTO samples demonstrated superior resistance, exhibiting the lowest corrosion current density, and lasting 31 % longer than the ones without high-temperature oxidation, and more than three times the least stable group with improper processing conditions. The degradation resistance arises from finer and more uniform grains, smoother surfaces, and the thicker stratified structure formed through oxidation. The processing route dictates the multi-level microstructure that governs degradation. The oxide layer and transition layer contribute to early-stage corrosion resistance due to the isolation of solutions and weakening of galvanic corrosion, while the size and distribution of equiaxed and columnar grains caused by the printing process dominate the longer-term degradation behavior of the Mg matrix. The “LPBF + HTO” process enables synergistic programming of complex porous Mg scaffolds with either “linear” (without oxidation) or “nonlinear” (with oxidation) degradation profiles, offering new insights in metal additive manufacturing for tailoring biodegradable scaffolds with tunable degradation kinetics.

These findings underscore the potential of process-informed microstructural engineering to overcome intrinsic limitations of Mg alloys, advancing the development of Mg alloys for orthopedic screws, bone regeneration scaffolds, and other load-bearing implants requiring tunable mechanical properties, biodegradation resistance, and biocompatibility [20,40,50]. Practically, this would suggest that manufacturers of biodegradable implants could optimize printing parameters in tandem with post-processing to obtain implants with predefined degradation timelines, potentially reducing the need for surface coatings and improving the reliability of Mg-based devices in clinical use. More broadly, our research addresses a critical research gap by linking layer-wise processing conditions to long-term degradation performance in Mg scaffolds, and offers a new paradigm for manufacturing-dominant control of biodegradation kinetics. This generalizable framework could be applied to other additive manufacturing materials where property control is critical (e.g., additively manufactured zinc or iron alloys).

Future work should explore dynamic immersion and *in vivo* testing of porous Mg scaffolds to confirm biocompatibility and mechanical integrity over implantation time. From a manufacturing standpoint, developing a predictive model for microstructure evolution during LPBF coupled with oxidation kinetics modeling could allow *a priori* optimization of process parameters for targeted degradation rates. Additionally, studies involving a statistical process control and long-term repeatability assessment (e.g., varying scaffold geometries and manufacturing batches) are needed to strengthen the conclusions.

CRediT authorship contribution statement

Weiyun Xu: Writing – original draft, Methodology, Conceptualization. **Hualuo Pang:** Writing – review & editing, Data curation. **Haojing Xu:** Visualization, Validation. **Jinge Liu:** Validation, Data curation. **Yufeng Zheng:** Supervision, Investigation. **Peng Wen:** Writing – review & editing, Supervision.

Declaration of generative AI and AI-assisted technologies in the manuscript preparation process

During the preparation of this work the authors used ChatGPT-5 for language polishing and style compliance. After using this tool/service, the authors reviewed and edited the content as needed and take full responsibility for the content of the published article.

Declaration of competing interest

The authors declare the following financial interests/personal relationships which may be considered as potential competing interests Peng Wen reports financial support was provided by National Natural Science Foundation of China. If there are other authors, they declare that they have no known competing financial interests or personal relationships that could have appeared to influence the work reported in this paper.

Acknowledgements

This work was supported by National Natural Science Foundation of China (52471262, 52175274). Jinge Liu acknowledges the support from Postdoctoral Science Foundation of China (2024M751653) and National Program for Postdoctoral Researchers of China (GZC20240845).

Appendix A. Supplementary data

Supplementary data to this article can be found online at <https://doi.org/10.1016/j.ijmachtools.2025.104362>.

Data availability

The raw data and scripts supporting the findings of this study are openly available on Mendeley Data at: doi 10.17632/frbfcmmyc4.1.

References

- [1] F. Witte, V. Kaese, H. Haferkamp, E. Switzer, A. Meyer-Lindenberg, C.J. Wirth, et al., In vivo corrosion of four magnesium alloys and the associated bone response, *Biomaterials* 26 (2005) 3557–3563, <https://doi.org/10.1016/j.biomaterials.2004.09.049>.
- [2] Y. Yang, C. He, E. Dianyu, W. Yang, F. Qi, D. Xie, et al., Mg bone implant: features, developments and perspectives, *Mater. Des.* 185 (2020), <https://doi.org/10.1016/j.matdes.2019.108259>.
- [3] K. Li, C. Ji, S. Bai, B. Jiang, F. Pan, Selective laser melting of magnesium alloys: necessity, formability, performance, optimization and applications, *J. Mater. Sci. Technol.* 154 (2023) 65–93, <https://doi.org/10.1016/j.jmst.2022.12.053>.
- [4] Y. Li, J. Zhou, P. Pavanram, M.A. Leeflang, L.I. Fockaert, B. Pouran, et al., Additively manufactured biodegradable porous magnesium, *Acta Biomater.* 67 (2018) 378–392, <https://doi.org/10.1016/j.actbio.2017.12.008>.
- [5] X. Zhang, X.W. Li, J.G. Li, X.D. Sun, Preparation and mechanical property of a novel 3D porous magnesium scaffold for bone tissue engineering, *Mater. Sci. Eng. C Mater Biol Appl* 42 (2014) 362–367, <https://doi.org/10.1016/j.msec.2014.05.044>.
- [6] M. Nasr Azadani, A. Zahedi, O.K. Bowoto, B.I. Oladapo, A review of current challenges and prospects of magnesium and its alloy for bone implant applications, *Prog. Biomater.* 11 (2022) 1–26, <https://doi.org/10.1007/s40204-022-00182-x>.
- [7] Y. Lu, S. Deshmukh, I. Jones, Y.L. Chiu, Biodegradable magnesium alloys for orthopaedic applications, *Biomater Transl* 2 (2021) 214–235, <https://doi.org/10.12336/biomatertransl.2021.03.005>.
- [8] N.A. Zumdicke, L. Jauer, L.C. Kersting, T.N. Kutz, J.H. Schleifenbaum, D. Zander, Additive manufactured WE43 magnesium: a comparative study of the microstructure and mechanical properties with those of powder extruded and as-cast WE43, *Mater. Char.* 147 (2019) 384–397, <https://doi.org/10.1016/j.matchar.2018.11.011>.
- [9] Y. Xin, T. Hu, P.K. Chu, In vitro studies of biomedical magnesium alloys in a simulated physiological environment: a review, *Acta Biomater.* 7 (2011) 1452–1459, <https://doi.org/10.1016/j.actbio.2010.12.004>.
- [10] Y. Wang, H. Huang, G. Jia, H. Zeng, G. Yuan, Fatigue and dynamic biodegradation behavior of additively manufactured Mg scaffolds, *Acta Biomater.* 135 (2021) 705–722, <https://doi.org/10.1016/j.actbio.2021.08.040>.
- [11] X. Wu, J. Liu, Y. Yang, J. Bai, C. Shuai, J. Buhagiar, et al., Laser powder bed fusion of biodegradable magnesium alloys: process, microstructure and properties, *Int. J. Extrem. Manuf.* 7 (2024), <https://doi.org/10.1088/2631-7990/ad967e>.
- [12] S. Sui, S. Guo, D. Ma, C. Guo, X. Wu, Z. Zhang, et al., Additive manufacturing of magnesium and its alloys: Process-formability-microstructure-performance relationship and underlying mechanism, *Int. J. Extrem. Manuf.* 5 (2023), <https://doi.org/10.1088/2631-7990/acf254>.
- [13] S. Zhao, M. Tayyebi, Mahdirezza Yarigarravesh, G. Hu, A review of magnesium corrosion in bio-applications: mechanism, classification, modeling, in-vitro, and in-vivo experimental testing, and tailoring Mg corrosion rate, *J. Mater. Sci.* 58 (2023) 12158–12181, <https://doi.org/10.1007/s10853-023-08782-z>.
- [14] S. Virtanen, Biodegradable Mg and Mg alloys: corrosion and biocompatibility, *Mater. Sci. Eng., B* 176 (2011) 1600–1608, <https://doi.org/10.1016/j.mseb.2011.05.028>.
- [15] J. Levorova, J. Dusкова, M. Drahos, R. Rvbova, D. Vojtech, J. Kubasek, et al., In vivo study on biodegradable magnesium alloys: bone healing around WE43 screws, *J. Biomater. Appl.* 32 (2018) 886–895, <https://doi.org/10.1177/0885328217743321>.
- [16] Y. Liu, B. Lu, Z. Cai, Recent progress on Mg- and Zn-Based alloys for biodegradable vascular stent applications, *J. Nanomater.* 1–16 (2019), <https://doi.org/10.1155/2019/1310792>.
- [17] K. Gusieva, C.H.J. Davies, J.R. Scully, N. Birbilis, Corrosion of magnesium alloys: the role of alloying, *Int. Mater. Rev.* 60 (2014) 169–194, <https://doi.org/10.1179/1743280414y.0000000046>.
- [18] J. Liu, S. Min, Z. Mao, M. Zhou, B. Liu, D. Liu, et al., Influence of high temperature oxidation on mechanical properties and in vitro biocompatibility of WE43 magnesium alloy fabricated by laser powder bed fusion, *J. Mater. Sci. Technol.* 179 (2024) 26–39, <https://doi.org/10.1016/j.jmst.2023.08.056>.
- [19] V. Karageorgiou, D. Kaplan, Porosity of 3D biomaterial scaffolds and osteogenesis, *Biomaterials* 26 (2005) 5474–5491, <https://doi.org/10.1016/j.biomaterials.2005.02.002>.
- [20] Y. Gu, Y. Liu, J. Buhring, L. Tian, M. Koblenzer, K.U. Schroder, et al., Biocompatibility and osteogenic capacity of additively manufactured biodegradable porous WE43 scaffolds: an in vivo study in a canine model, *Biomater. Adv.* 164 (2024) 213984, <https://doi.org/10.1016/j.bioadv.2024.213984>.
- [21] M. Yazdimamaghani, M. Razavi, D. Vashaei, K. Moharamzadeh, A.R. Boccaccini, L. Tayebi, Porous magnesium-based scaffolds for tissue engineering, *Mater. Sci. Eng. C Mater Biol Appl* 71 (2017) 1253–1266, <https://doi.org/10.1016/j.msec.2016.11.027>.
- [22] M. Yang, X. Liu, Z. Zhang, Y. Song, Stress corrosion behavior of AM50Gd magnesium alloy in different environments, *Metals* 9 (2019), <https://doi.org/10.3390/met9050616>.
- [23] J. Zhang, S. Xie, T. Li, Z. Liu, S. Zheng, H. Zhou, A study of multi-stage energy absorption characteristics of hybrid sheet TPMS lattices, *Thin-Walled Struct.* 190 (2023), <https://doi.org/10.1016/j.tws.2023.110989>.
- [24] A. du Plessis, S.M.J. Razavi, M. Benedetti, S. Murchio, M. Leary, M. Watson, et al., Properties and applications of additively manufactured metallic cellular materials: a review, *Prog. Mater. Sci.* 125 (2022), <https://doi.org/10.1016/j.pmatsci.2021.100918>.
- [25] S.K. Manjhi, P. Sekar, S. Bontha, A.S.S. Balan, Additive manufacturing of magnesium alloys: characterization and post-processing, *Int. J. Lightweight Mater. Manuf.* 7 (2024) 184–213, <https://doi.org/10.1016/j.ijlmm.2023.06.004>.
- [26] J. Chen, B. Chen, Progress in additive manufacturing of magnesium alloys: a review, *Materials* 17 (2024), <https://doi.org/10.3390/matl7153851>.
- [27] K. V. N. Kumar B, S. Kumar S, V. M, Magnesium role in additive manufacturing of biomedical implants – challenges and opportunities, *Addit. Manuf.* 55 (2022), <https://doi.org/10.1016/j.addma.2022.102802>.
- [28] M. Esmaily, Z. Zeng, A.N. Mortazavi, A. Gullino, S. Choudhary, T. Derra, et al., A detailed microstructural and corrosion analysis of magnesium alloy WE43 manufactured by selective laser melting, *Addit. Manuf.* 35 (2020), <https://doi.org/10.1016/j.addma.2020.101321>.
- [29] J. Liu, B. Lu, S. Min, B. Yin, B. Peng, Z. Yu, et al., Biodegradable magnesium alloy WE43 porous scaffolds fabricated by laser powder bed fusion for orthopedic applications: process optimization, in vitro and in vivo investigation, *Bioact. Mater.* 16 (2022) 301–319, <https://doi.org/10.1016/j.bioactmat.2022.02.020>.
- [30] F. Bar, L. Berger, L. Jauer, G. Kurtuld, R. Schaublin, J.H. Schleifenbaum, et al., Laser additive manufacturing of biodegradable magnesium alloy WE43: a detailed microstructure analysis, *Acta Biomater.* 98 (2019) 36–49, <https://doi.org/10.1016/j.actbio.2019.05.056>.
- [31] J. Soderlind, A.A. Martin, N.P. Calta, P.J. DePond, J. Wang, B. Vrancken, et al., Melt-pool dynamics and microstructure of Mg Alloy WE43 under laser powder bed fusion additive manufacturing conditions, *Crystals* 12 (2022), <https://doi.org/10.3390/cryst12101437>.
- [32] B. Yin, K. Li, W. Chen, H. Huang, D. Liu, F. Song, et al., Effect of powder composition on WE43 magnesium alloy fabricated by laser powder bed fusion, *J. Mater. Res. Technol.* 32 (2024) 577–588, <https://doi.org/10.1016/j.jmrt.2024.07.166>.
- [33] B. Yin, J. Liu, B. Peng, M. Zhou, B. Liu, X. Ma, et al., Influence of layer thickness on formation quality, microstructure, mechanical properties, and corrosion resistance of WE43 magnesium alloy fabricated by laser powder bed fusion, *J. Magnesium Alloys* 12 (2024) 1367–1385, <https://doi.org/10.1016/j.jma.2022.09.016>.
- [34] M.A. Hafeez, A. Farooq, A. Zang, A. Saleem, K.M. Deen, Phosphate chemical conversion coatings for magnesium alloys: a review, *J. Coating Technol. Res.* 17 (2020) 827–849, <https://doi.org/10.1007/s11998-020-00335-2>.
- [35] G. Barati Darband, M. Aliofkharzai, P. Hamghalam, N. Valizade, Plasma electrolytic oxidation of magnesium and its alloys: mechanism, properties and applications, *J. Magnesium Alloys* 5 (2017) 74–132, <https://doi.org/10.1016/j.jma.2017.02.004>.
- [36] M. Li, F. Benn, T. Derra, N. Kroger, M. Zinser, R. Smeets, et al., Microstructure, mechanical properties, corrosion resistance and cytocompatibility of WE43 Mg

- alloy scaffolds fabricated by laser powder bed fusion for biomedical applications, *Mater Sci Eng C Mater Biol Appl* 119 (2021) 111623, <https://doi.org/10.1016/j.msec.2020.111623>.
- [37] A. Hanzi, P. Gunde, M. Schinhammer, P. Uggowitzer, On the biodegradation performance of an Mg–Y–RE alloy with various surface conditions in simulated body fluid, *Acta Biomater.* 5 (2009) 162–171, <https://doi.org/10.1016/j.actbio.2008.07.034>.
- [38] P.-W. Chu, E.A. Marquis, Linking the microstructure of a heat-treated WE43 Mg alloy with its corrosion behavior, *Corros. Sci.* 101 (2015) 94–104, <https://doi.org/10.1016/j.corsci.2015.09.005>.
- [39] J. Liu, B. Yin, F. Song, B. Liu, B. Peng, P. Wen, et al., Improving corrosion resistance of additively manufactured WE43 magnesium alloy by high temperature oxidation for biodegradable applications, *J. Magnesium Alloys* 12 (2024) 940–953, <https://doi.org/10.1016/j.jma.2022.08.009>.
- [40] B. Liu, J. Liu, C. Wang, Z. Wang, S. Min, C. Wang, et al., High temperature oxidation treated 3D printed anatomical WE43 alloy scaffolds for repairing periarticular bone defects: in vitro and in vivo studies, *Bioact. Mater.* 32 (2024) 177–189, <https://doi.org/10.1016/j.bioactmat.2023.09.016>.
- [41] Q. Huang, S. Yu, Y. Chen, S. Lu, Z. Lu, C. Liu, Study on the high temperature oxidation/nitridation behavior of Mg alloys AZ31, WE43 and ZE10, *Case Stud. Therm. Eng.* 30 (2022), <https://doi.org/10.1016/j.csite.2022.101759>.
- [42] Y. Qin, P. Wen, H. Guo, D. Xia, Y. Zheng, L. Jauer, et al., Additive manufacturing of biodegradable metals: current research status and future perspectives, *Acta Biomater.* 98 (2019) 3–22, <https://doi.org/10.1016/j.actbio.2019.04.046>.
- [43] B. Hu, J. Han, Z. Jiang, F. Yao, M. Yu, Y. Zhao, et al., Flame ignition mechanism of magnesium alloys controlled by oxide films based on the oxidation behaviors of Al, Nd and Y, *J. Mater. Sci. Technol.* 212 (2025) 123–138, <https://doi.org/10.1016/j.jmst.2024.06.021>.
- [44] J. Han, B. Hu, Z. Jiang, F. Yao, Z. Li, D. Li, et al., Recent advances on the oxide film of ignition-proof magnesium alloys: a review, *J. Magnesium Alloys* 13 (2025) 4–29, <https://doi.org/10.1016/j.jma.2024.05.018>.
- [45] T. Liang, J. Liu, C. Zhan, S. Peng, J. Pu, Effect of yttrium oxide on microstructure and oxidation behavior of Cr/FeCrAl coatings fabricated by extreme high-speed laser cladding process: an experimental approach, *Materials* 18 (2025), <https://doi.org/10.3390/ma18081821>.
- [46] W. Ali, M. Li, L. Tillmann, T. Mayer, C. Gonzalez, L.L. J., et al., Bioabsorbable WE43 Mg alloy wires modified by continuous plasma-electrolytic oxidation for implant applications. Part I: processing, microstructure and mechanical properties, *Biomater. Adv.* 146 (2023) 213314, <https://doi.org/10.1016/j.bia.2023.213314>.
- [47] A. Stern, G. Barzani, Autogenous bone harvest for implant reconstruction, *Dent. Clin.* 59 (2015) 409–420, <https://doi.org/10.1016/j.cden.2014.10.011>.
- [48] A. Kopp, T. Derra, M. Muther, L. Jauer, J.H. Schleifenbaum, M. Voshage, et al., Influence of design and postprocessing parameters on the degradation behavior and mechanical properties of additively manufactured magnesium scaffolds, *Acta Biomater.* 98 (2019) 23–35, <https://doi.org/10.1016/j.actbio.2019.04.012>.
- [49] G. Dai, Z. Sun, Y. Li, J. Jain, A. Bhownik, J. Shinjo, et al., Grain refinement and columnar-to-equiaxed transition of Ti6Al4V during additive manufacturing via different laser oscillations, *Int. J. Mach. Tool Manuf.* 189 (2023), <https://doi.org/10.1016/j.ijmachtools.2023.104031>.
- [50] J. Draxler, E. Martinelli, A.M. Weinberg, A. Zitek, J. Irrgeher, M. Meischel, et al., The potential of isotopically enriched magnesium to study bone implant degradation in vivo, *Acta Biomater.* 51 (2017) 526–536, <https://doi.org/10.1016/j.actbio.2017.01.054>.